Materials Today Bio 32 (2025) 101634

Contents lists available at ScienceDirect

Materials Today Bio

journal homepage: www.journals.elsevier.com/materials-today-bio

Oxymatrine and astragaloside IV co-loaded liposomes: Scale-up purposes and their enhancement of anti-PD-1 efficacy against breast cancer

Liangyin Wei [a,b,1], Hong Wang [a,b,1], Xietao Ye [a,b,1], Junfan Yue [a,b], Hong Guo [a,b], Dengxuan Mao [a,b], Xia Li [a,b], Yeyang Sun [a,b], Congyan Liu [a,b], Yuping Liu [a,b,*], Yan Chen [a,b,**]

[a] Affiliated Hospital of Integrated Traditional Chinese and Western Medicine, Nanjing University of Chinese Medicine, Nanjing 210028, China
[b] Multi-component of Traditional Chinese Medicine and Microecology Research Center, Jiangsu Province Academy of Traditional Chinese Medicine, Nanjing 210028, China

ARTICLE INFO

Keywords:
Oxymatrine
Astragaloside IV
Co-loaded liposomes
Microfluidics
Tumor-infiltrating T lymphocytes
PD-1 inhibitors

ABSTRACT

The response rate of programmed cell death protein-1 (PD-1) inhibitors in breast cancer remains unsatisfactory, primarily due to the limited infiltration and activity of tumor-infiltrating T lymphocytes (TILs). Previous studies demonstrated that oxymatrine (Om) and astragaloside IV (As) could enhance TIL infiltration and function by inhibiting cancer-associated fibroblasts (CAFs) and promoting mitochondrial activity in TILs, respectively. Thus, combining Om and As may be a promising strategy to improve the antitumor effects of PD-1 inhibitors in breast cancer. However, co-delivery above drugs into breast cancer tissue is challenging due to their low bioavailability and distinct physicochemical properties. This study addresses this challenge by formulating Om and As co-loaded liposomes (Om-As-Lip) and comparing the scale-up production methods: high-pressure homogenization (EP-HPH) and microfluidics. Om-As-Lip prepared *via* microfluidics demonstrated superior entrapment efficiency (As: 99.03 ± 0.04 %, Om: 67.01 ± 0.02 %) and a significantly higher production rate (22.12 mL/min) compared to EP-HPH (1.19 mL/min). Additionally, Om-As-Lip produced by microfluidics increased the area under the curve (AUC) (Om: 6.17-fold, As: 2.07-fold) and maximum concentration (Cmax) (Om: 1.58-fold, As: 3.49-fold) compared to the free drugs. Importantly, Om-As-Lip enhanced the antitumor efficacy of α-PD-1 by inhibiting CAF activation and boosting TIL activity, resulting in a tumor inhibition rate of 61.2 % and extended survival in mice. This work presents a novel perspective for scaling up co-delivered formulations of drugs with differing polarities to improve breast cancer immunotherapy.

1. Introduction

In recent years, immunotherapy using programmed cell death protein 1 (PD-1) inhibitors has recently been regarded as a potent treatment for breast cancer due to its sustained therapeutic efficacy and safety profile [1–3]. However, only a limited number of patients demonstrate a positive response to this therapy [4]. Research indicates that the poor response rate to PD-1 inhibitors in breast cancer is largely caused by the insufficient presence and impaired function of tumor-infiltrating lymphocytes (TILs) [5]. On one hand, cancer-associated fibroblasts (CAFs) within the breast cancer create physical barriers that impede TIL infiltration [6]. On the other hand, the metabolic stress induced by the breast cancer microenvironment disrupts mitochondrial function in TILs [7], thereby diminishing their activity and compromising the efficacy of PD-1 inhibitors. Enhancing TIL levels and activity by inhibiting CAF activation and restoring mitochondrial function in TILs could therefore improve the therapeutic efficacy of PD-1 inhibitors.

Our previous studies have demonstrated that oxymatrine (Om), a hydrophilic quinolizidine alkaloid from *Sophora flavescens*, effectively inhibits CAF activation and promotes TIL infiltration in the tumor [8–10]. Astragaloside IV (As), a hydrophobic triterpenoid glycoside from *Astragalus membranaceus Bunge*, enhances mitochondrial function in TILs, boosting their secretion of anti-tumor cytokines [7]. Therefore, the combination of Om and As holds promise for increasing PD-1

* Corresponding author. Affiliated Hospital of Integrated Traditional Chinese and Western Medicine, Nanjing 210028, China.
** Corresponding author. Affiliated Hospital of Integrated Traditional Chinese and Western Medicine, Nanjing 210028, China.
E-mail addresses: liuyuping@jsatcm.com (Y. Liu), chenyan@jsatcm.com (Y. Chen).
[1] L Wei, H Wang and X Ye contributed equally.

https://doi.org/10.1016/j.mtbio.2025.101634
Received 13 January 2025; Received in revised form 23 February 2025; Accepted 2 March 2025
Available online 4 March 2025

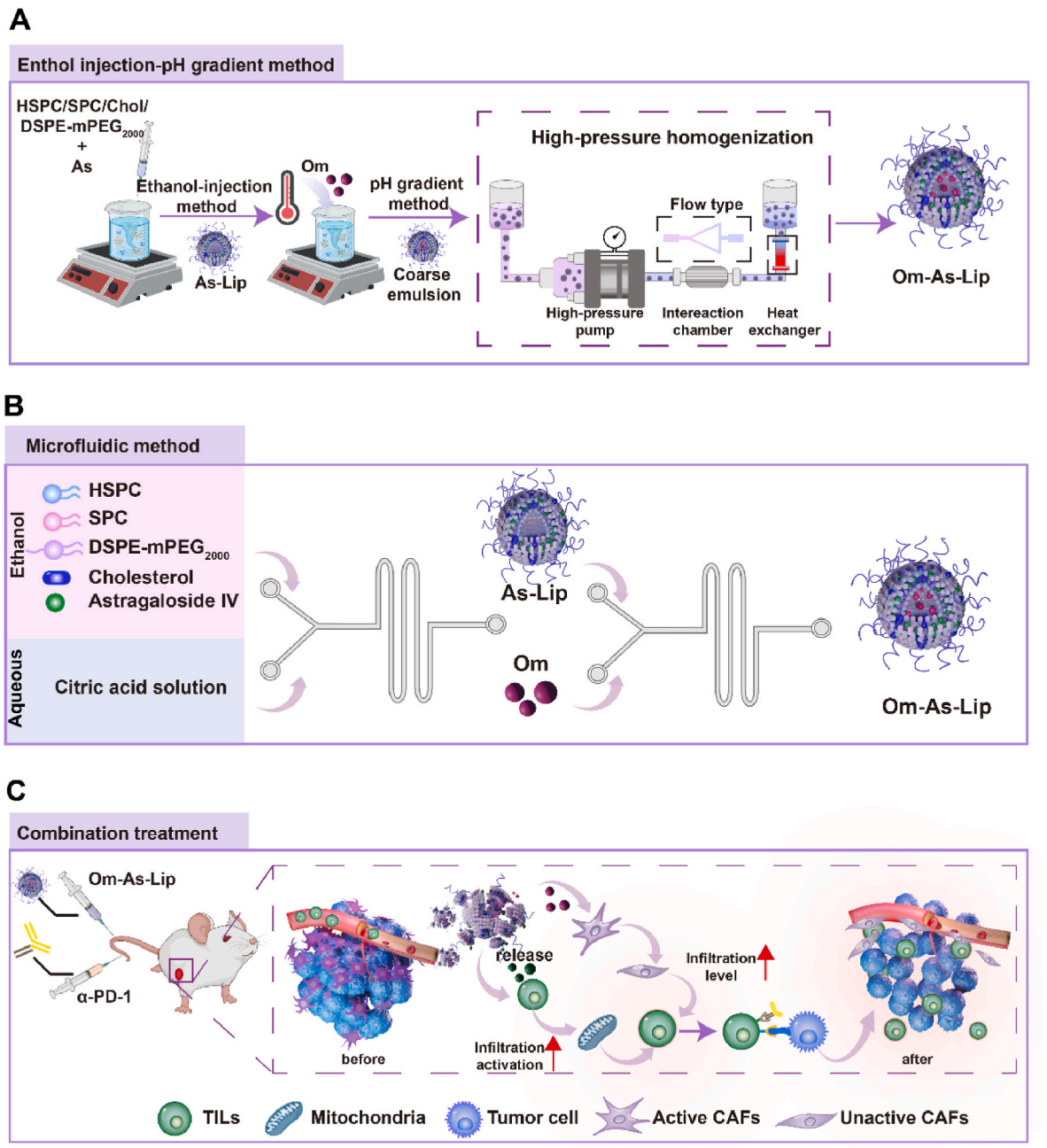

Fig. 1. Schematic illustration of the preparation and *in vivo* performance of Om-As-Lip for enhancing breast cancer immunotherapy. (A) Om-As-Lip prepared using the EP-HPH method. (B) Om-As-Lip prepared using the microfluidic method. (C) Om-As-Lip co-delivers Om and As into the breast cancer microenvironment, promoting TIL infiltration and activity, thereby improving the efficacy of PD-1 inhibitors.

inhibitor efficacy by simultaneously enhancing TIL infiltration and activity in breast cancer [7,11,12]. Nevertheless, the distinct polarity and limited bioavailability of Om and As present significant challenges for their co-delivery into breast cancer tissue [13–16].

In response to this challenge, a range of nanoplatforms has been developed to co-deliver multiple drugs, improving their bioavailability and tumor accumulation [17–19]. Liposomes, which consist of a lipid bilayer surrounding an aqueous core, offer a promising solution for co-encapsulating drugs with differing properties, presenting an attractive prospect for industrial-scale manufacturing [20,21]. This structure enables the encapsulation of hydrophilic drugs like Om in the core and hydrophobic drugs like As within the lipid bilayer [22,23]. However, successful development and clinical translation of liposomal products have been limited, primarily focusing on drugs with similar polarity, such as CPX-351, which co-loads two hydrophilic agents, cytarabine and daunorubicin. Research on liposomes co-encapsulating drugs with varying polarities remains scarce, as it demands a deep understanding of formulation and process variables. Minor adjustments in the formulation or production process can significantly affect the final liposomal properties [24,25]. Therefore, not only is the preparation of liposomes co-delivering Om and As at a laboratory scale challenging, but its large-scale production is an even greater challenge [26].

Currently, two primary scale-up strategies are employed for liposome fabrication: top-down and bottom-up approaches. The top-down approaches involve high-energy processes that reduce liposome particle sizes to the nanometer range [27]. These approaches have been successfully applied in both laboratory and commercial-scale production, with size homogenization steps such as high-pressure

homogenization (HPH) typically required to achieve the desired size and polydispersity [28]. However, this traditional method often involves multiple steps, resulting in extended production times and lower reproducibility [29]. In contrast, bottom-up methods, exemplified by microfluidics, have emerged as a promising fabrication technology, capable of producing liposomes quickly and with high reproducibility. Despite the rapid development of microfluidic platforms, the co-loading of hydrophilic and hydrophobic drugs in liposomes remains challenging.

In this study, a liposomal formulation was developed to co-encapsulate the water-soluble drug oxymatrine (Om) and the water-insoluble drug astragaloside IV (As) (Om-As-Lip), aiming to enhance the antitumor efficacy of PD-1 inhibitors. This study optimized the formulation and process parameters at the laboratory scale and subsequently compared the scale-up production of liposomes using EP-HPH with those produced by microfluidics (Fig. 1A and B). Liposomes prepared *via* both methods demonstrated appropriate size, but Om-As-Lip produced by microfluidics showed superior drug entrapment efficiency, indicating its potential for large-scale production. Additionally, microfluidic-prepared Om-As-Lip significantly increased the area under the curve (AUC) compared to the free drug. The formulation also modulated the breast cancer microenvironment by inhibiting CAF activation and restoring mitochondrial function in TILs, thereby enhancing both the quantity and activity of TILs, ultimately improving the efficacy of PD-1 inhibitors (Fig. 1C). In conclusion, this study provides a scalable manufacturing process for Om and As co-loaded liposomes, offering promising potential for clinical applications in breast cancer immunotherapy.

2. Materials and methods

2.1. Materials, cell lines, and animals

Astragaloside IV (>98 %) was sourced from Shanghai Yuanye Bio-Technology Co., Ltd. (Shanghai, China), and oxymatrine (>98 %) was provided by Nanjing Spring & Autumn Biological Engineering Co., Ltd. (Nanjing, China). Hydrogenated phosphatidylcholine from soybeans (HSPC, ≥98 %), soybean phosphatidylcholine (SPC, >80 %), and egg phospholipids (EPC, >98 %) were purchased from AVT Pharmaceutical Technology Co., Ltd. (Shanghai, China). Cholesterol (>99 %) and 1,2-distearoyl-sn-glycero-3-phosphoethanolamine-N-[methoxy(polyethylene glycol)-2000] (DSPE-PEG_{2000}, >98 %) were obtained from Rhawn Technology Co., Ltd. (Shanghai, China). Coumarin 6 (C6) and lissamine rhodamine B (SRB) were purchased from Aladdin Reagent Co., Ltd (Shanghai, China). DiD was obtained from Shanghai Yien Chemical Technology Co., Ltd. (Shanghai, China). *In vivo* MAb anti-mouse PD-1 was provided from BioXcell Co., Ltd. (New Hampshire, America). All other reagents were of analytical grade or higher and were commercially sourced.

CTLL-2 (mouse T lymphocytes) and 4T1-luc cells (luciferase-labeled mouse breast cancer cells) were obtained from the American Type Culture Collection (ATCC) and cultured in RPMI 1640 medium (Gibco) supplemented with 10 % fetal bovine serum (FBS, SORFA). NIH3T3 cells (mouse embryonic fibroblasts), also from ATCC, were cultured in Dulbecco's modified Eagle's medium (DMEM, Gibco) containing 10 % FBS. Cells were maintained in a humidified incubator at 37 °C with 5 % CO_2 and passaged every 2–3 days.

Female BALB/c mice were purchased from GemPharmatech LLC (Nanjing, China) and housed under pathogen-free conditions. Mice were used for experiments at 6–8 weeks of age, with all experimental protocols approved by the Animal Experimentation Ethics Committee of Jiangsu Provincial Academy of Traditional Chinese Medicine (AEWC-20211105-170).

2.2. Preparation of liposomes

For lab-scale production, As-Lip (As-loaded liposome) was initially prepared using either the thin film hydration method or the ethanol injection method, while Om-Lip (Om-loaded liposome) was prepared *via* the pH/ammonium sulfate method. Om-As-Lip, co-loaded with As and Om, was subsequently prepared by combining the ethanol injection method with the pH gradient method. Specifically, 1.5 mg As, 52.0 mg HSPC, 9.0 mg SPC, 10.6 mg cholesterol, and 2.5 mg DSPE-$mPEG_{2000}$ were dissolved in 2 mL ethanol and injected into 5 mL of citric acid solution (300 mmol/L) under stirring at 60 °C. Ethanol was evaporated at 50 °C until no odor remained, yielding the As-Lip solution. Afterward, 1 mL of HEPES buffer (50 mmol/L) was added to the As-Lip solution, followed by 4 mL of Na_2CO_3 solution (300 mmol/L) containing 2.5 mg Om. The pH was adjusted to 7.0, resulting in the formation of Om-As-Lip.

For scale-up, Om-As-Lip was produced by combining the ethanol injection method with the pH gradient method, followed by either the EP-HPH (high-pressure homogenization) process or a microfluidic process.

EP-HPH process: The scale-up process based on the lab-scale method with a 150-fold increase in formulation, producing a 1.5 L batch of coarse emulsion. Homogenization was conducted at 600 bar for six cycles using a high-pressure homogenizer at 4 °C, yielding the homogenized liposomes.

Microfluidic process: The microfluidic system employed a staggered herringbone microfluidic chip on an LNP-S1 smart LNP synthesizer (Fluidiclab, China). The chip featured two inlet channels for the aqueous phase and lipid solution and one outlet channel. Lipids (HSPC, SPC, DSPE-$mPEG_{2000}$, cholesterol) and As were dissolved in ethanol at the same concentrations as in the lab-scale process, while citric acid solution (300 mmol/L) served as the aqueous buffer. The flow rate ratio (FRR) between the aqueous and solvent streams was adjusted from 1:1 to 1:8, with the total flow rate (TFR) varying between 8 and 16 mL/min, and the total volume (TV) ranging from 4 to 12 mL. After each run, As-Lip was collected at the outlet chamber. As-Lip and Na_2CO_3 solution (300 mmol/L, containing Om) were then injected into the solvent channel to produce Om-As-Lip. Before mixing, the FRR was adjusted from 1:1 to 1:8 (solvent: aqueous ratio), the TFR was set between 5 and 16 mL/min, and the TV ranged from 5 to 12 mL. The final Om-As-Lip was collected after ethanol removal *via* ultrafiltration.

2.3. Characterization of liposomes

The particle size, polydispersity index (PDI), and zeta potential of the liposomes were determined using dynamic light scattering (DLS, Nano ZS90 Zetasizer, Malvern). Liposome morphology was examined by transmission electron microscopy (TEM) with a Tecnai-12 microscope (FEI, USA) at an accelerating voltage of 120 kV.

Encapsulation efficiency (EE) and drug-loading (DL) were quantified using high-pressure liquid chromatography (HPLC, Agilent 1260, USA) and calculated with the following formulas:

$$EE\,(\%) = (\text{Amount of drug in liposomes} \,/\, \text{Total amount of drug}) \times 100\%$$

$$DL\,(\%) = [\text{Amount of drug in liposomes} \,/\, (\text{Amount of drug in liposomes} + \text{Amount of lipids})] \times 100\%$$

Om was quantified by HPLC using a Supersil ODS2-C18 (150 mm × 4.6 mm, 5 μm) column, with UV detection at 220 nm. The mobile phase consisted of 0.1 % phosphoric acid and 0.16 % triethylamine in water, combined with acetonitrile (90:10, v/v), at a flow rate of 0.8 mL/min. As was quantified using the same chromatographic system with a 6100-Evaporative Light Scattering Detector (ELSD, Alltech, USA), using a mobile phase of water and acetonitrile (65:35, v/v), with a flow rate of 1.0 mL/min through the same column. Lipid components (HSPC, DSPE-mPEG$_{2000}$, cholesterol, and SPC) were detected by ELSD. The separation process and validation details are provided in Supplementary Table 1.

Lipid composition (HSPC, SPC, DSPE-mPEG$_{2000}$, and cholesterol) was analyzed using HPLC-ELSD with an Agilent Zorbax Eclipse Plus C18 (4.6 × 100 mm, 3.5 μm) column preheated to 30 °C. The mobile phase consisted of two components: Solution A, which was a 20 mM ammonium acetate buffer, and Solution B, methanol, with a flow rate of 1 mL/min (Supplementary Table 1).

To validate the co-encapsulation of hydrophilic and hydrophobic agents, fluorescent dyes SRB (hydrophilic) and C6 (hydrophobic) were used as substitutes for Om and As, respectively. The resulting SRB-C6-Lip was imaged using a TCS SP8 confocal laser scanning microscope (Leica, Germany) with excitation wavelengths of 488 nm and 561 nm for FITC and PE, respectively.

Differential scanning calorimetry (DSC) thermograms of liposomes were recorded using a TA-DSC (NETZSCH, Germany). Samples (Om-As-Lip, blank liposomes, Om-As, and physical mixtures of drugs and lipid components) were sealed in aluminum pans. Heating scans were conducted from −20 °C to 80 °C at 5 °C/min under nitrogen flow. An empty aluminum pan served as the reference, and each sample was measured in triplicate.

Liposome viscosity was measured using an NDJ-5S rotational rheometer (Yueping, China), and pH values were determined with a PB-10 pH meter (Sartorius, Germany). All measurements were performed in triplicate at room temperature.

2.4. In vitro drug release

The dialysis method was used to evaluate the release profile of Om-As-Lip. A 5 mL sample of each formulation was placed into a dialysis bag with a 10 kD molecular weight cutoff, and the dialysis was conducted in 150 mL phosphate-buffered saline (PBS) at different pH values (5.0, 6.5, and 7.4) containing 0.5 % Tween-80. The dialysis system was maintained at 37 °C with constant shaking at 100 rpm. At predetermined intervals, 1 mL of the external medium was withdrawn and replaced with fresh medium. The cumulative release of Om and As from the liposomes was quantified by HPLC. Each experiment was performed in triplicate.

2.5. Stability study

Storage stability: The stability of Om-As-Lip was assessed by storing the suspension at 4 °C for 60 days, during which particle size, PDI, zeta potential, Om and As content, and lipid composition (HSPC, SPC, cholesterol, and DSPE-mPEG$_{2000}$) were periodically measured.

Chemical stability: The chemical stability of Om-As-Lip was determined by monitoring peroxide value (PV) and acid value over 60 days [30].

2.6. In vitro experiments

2.6.1. Transwell migration assay

NIH3T3 cells (2 × 10^3 cells/well) were seeded onto 5.0 μm transwell plates (Corning) and incubated for 24 h. Following this, Om-As or Om-As-Lip was added to the wells, and after 2 h, 5 ng/mL TGF-β1 (Novoprotein) was introduced to induce CAF formation. After 24 h, the upper chamber medium was replaced. CTLL-2 cells (1 × 10^6, 1 % FBS RPMI 1640) were added to the upper chamber, while the lower chamber was filled with 20 % FBS RPMI 1640. After 3 h, cells in the lower chamber were collected in 100 μL RPMI 1640 for further quantification.

2.6.2. Cell uptake assessment

Cellular uptake was examined through fluorescence microscopy and flow cytometry. 4T1 cells were seeded in 6-well plates at a density of 5 × 10^4 cells per well and incubated at 37 °C with 5 % CO_2 overnight. Fluorescently labeled liposomes (SRB and C6) and free SRB-C6 were added to the cells. At various time points (2 h, 4 h, 6 h, 8 h, 12 h, 24 h), the medium was removed, and cells were washed three times with cold PBS. Cells were then observed under a fluorescence microscope (IX-73, Olympus). For quantification, the cells were washed, centrifuged, and analyzed using the A00-1-1101 Cyto FLEX (BECKMAN Coulter, USA).

The cellular uptake mechanism of SRB-C6-Lip was explored by flow cytometry. Cells were pretreated with inhibitors such as sucrose, genistein, and amiloride and exposed to 4 °C conditions. SRB-C6-Lip and free SRB-C6 were then incubated with the cells, and flow cytometry was used to assess drug uptake mechanism.

2.7. In vivo experiments

2.7.1. Pharmacokinetics and biodistribution study

4T1-luc cells (1 × 10^6 cells per mouse) were orthotopically injected into the fat pad of BALB/c mice to establish a breast cancer model. For pharmacokinetics analysis, the mice were administered the following formulations intravenously *via* the tail vein: (1) Om-As and (2) Om-As-Lip (2.0 mg/kg Om and 1.5 mg/kg As). Blood samples were collected at predetermined time points (0, 0.166, 0.25, 0.5, 0.75, 1, 2, 4, 6, 8, 12, 24 h) and centrifuged for 5 min at 4000 rpm. Plasma concentrations of Om and As were measured using ultra-performance liquid chromatography-tandem mass spectrometry (UPLC-MS-MS, Sciex, USA), with analytical conditions detailed in Tables S1–S3.

For tissue quantification of Om and As, samples from the liver, kidneys, spleen, lungs, heart, and tumor were collected at specific time points (1, 2, 4, 6, 8, 10, 12, 24 h) post-administration. The tissues were weighed, suspended in 1 mL of cold methanol, and homogenized at 4 °C. The homogenates were centrifuged at 12,000 rpm for 10 min at 4 °C, and the supernatant was collected into 5 mL EP tubes. The precipitates were resuspended in 1 mL of cold chloroform, homogenized, and centrifuged again at 12,000 rpm for 10 min at 4 °C. The resulting supernatants were combined for further analysis.

The biodistribution was assessed using fluorescence imaging. Mice were intravenously injected with either DiD or DiD-Lip, and images were captured at various time points (1, 4, 8, 12, and 24 h) using the IVIS Spectrum system. At 24 h post-injection, the mice were sacrificed, and tumors along with major organs (heart, liver, spleen, lungs, kidneys) were harvested for *ex vivo* imaging using the Living Image 4.4 system (PerkinElmer, USA) with excitation at 680 nm and emission at 710 nm. The DiD fluorescence intensity in the tissues was quantified and compared.

2.7.2. Antitumor efficacy

To assess the antitumor efficacy of Om-As-Lip, orthotopic 4T1-luc tumor models were generated and the mice were randomly allocated into five groups ($n = 6$): Model, Om-As, α-PD-1, Om-As-Lip, and Om-As-Lip combined with α-PD-1. After 3 days, Om and As or Om-As-Lip were administered intravenously (Om 2.0 mg/kg, As 1.5 mg/kg). For groups receiving α-PD-1 or the combination treatment, α-PD-1 (5 mg/kg) was injected intravenously every 4 days. Tumor volume was calculated daily based on the longest surface length (L) and width (W) measured with a caliper. At the end of the study, mice were euthanized, and tumor weights were recorded. Additionally, tumor sections were stained with HE, Ki67, and TUNEL for histopathological examination.

Survival analysis was conducted by recording the time of death for each mouse, and the median survival was calculated.

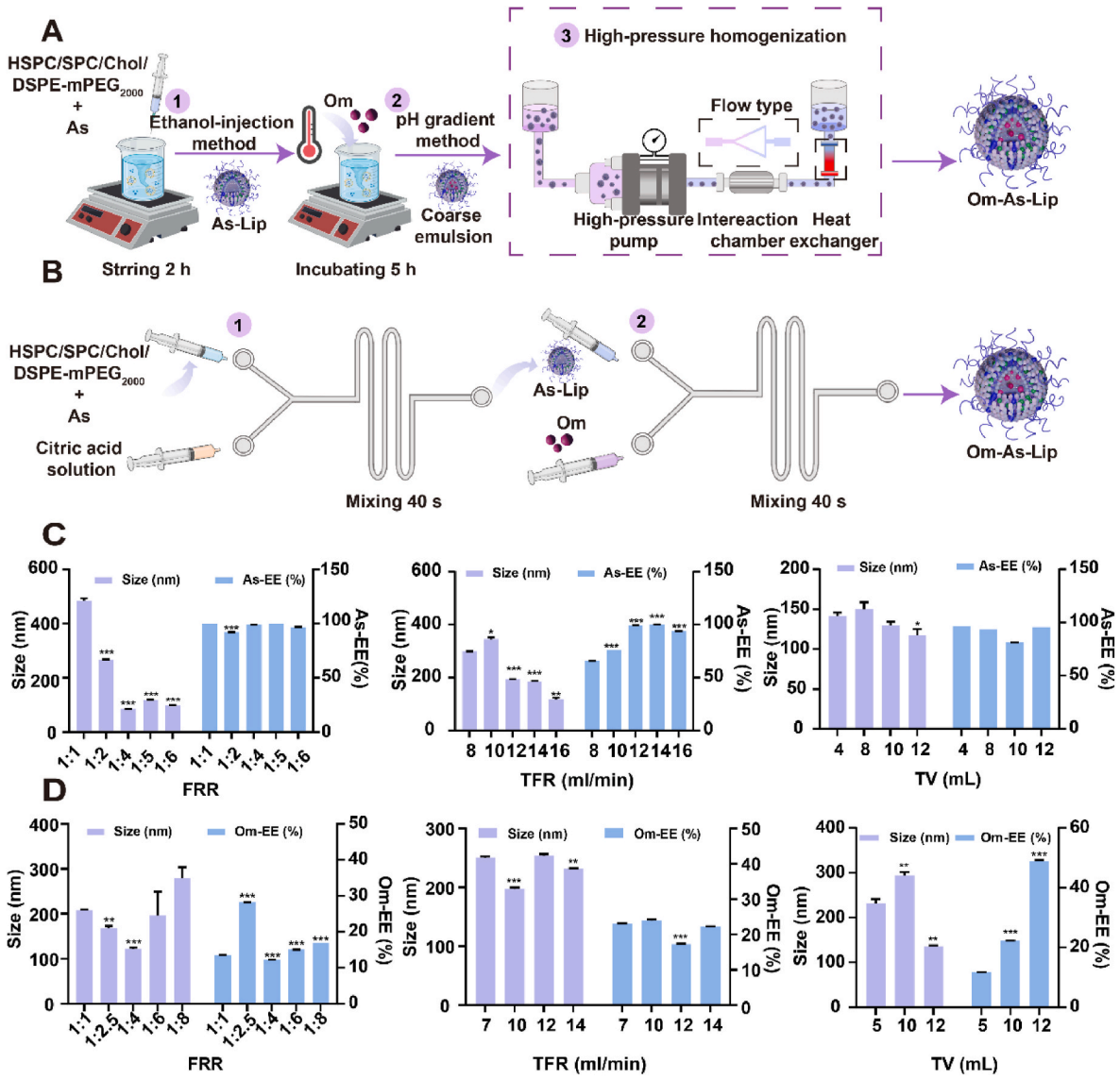

Fig. 2. (A) The EP-HPH process involves three key steps: 1) Preparation of As-Lip using the ethanol-injection method; 2) Active loading of Om into As-Lip *via* the pH gradient method; 3) Size reduction through the HPH method. (B) The microfluidic process consists of two primary steps: 1) As-Lip is formed by mixing the lipid solution (containing As) with a citric acid buffer in a microfluidic chip; 2) Om-As-Lip is produced by combining As-Lip with Na_2CO_3 solution (containing Om) in the microfluidic chip. (C) The impact of different parameters (FRR, TFR, TV) on the size and As-EE of As-Lip. (D) The influence of different parameters (FRR, TFR, TV) on the size and Om-EE of Om-As-Lip. (Data presented as Mean ± SD, *p*-value: $^*p < 0.05$, $^{**}p < 0.01$, $^{***}p < 0.001$; ns indicates not significant).

2.7.3. Flow cytometry analysis

Tumor tissues were excised, minced, and digested using a mixture of DNA I enzyme (0.04 mg/mL), collagenase I (1 mg/mL), collagenase IV (1 mg/mL), and hyaluronidase (0.4 mg/mL) from Biofroxx. The digestion process occurred at 37 °C for 3 h, after which the suspension was filtered through a 40 μm cell strainer. Cell concentration was adjusted to 1×10^7 cells/mL, and 100 μL aliquots were stained according to the manufacturer's protocol to identify specific cell populations.

For flow cytometry analysis, the following fluorescently labeled anti-mouse antibodies were used: Fixable Viability Zombie Aqua Fixable Viability Kit, anti-CD45-APC-A750, anti-CD3-APC, anti-CD4-PC-7, and anti-CD8-PE (BioLegend). Cells were stained with surface antibodies for 30 min at 4 °C and analyzed using a CytoFlex S flow cytometer. FlowJo software was used for data analysis.

2.8. Western blotting

Levels of α-SMA and FAP were evaluated through Western blotting. Protein was extracted using RIPA buffer, and 50 μg of each sample was electrophoresed on 10 % SDS-PAGE gels, followed by transfer to PVDF membranes. Membranes were blocked with 5 % BSA and probed with antibodies for FAP (Affinity, China), α-SMA (Abcam, USA), and GAPDH (Bioworld, China), with GAPDH as the loading control. Image analysis was performed using Image J 3.2.

2.9. Cellular immunofluorescence

FAP levels were further analyzed through immunofluorescence. Cells were washed with PBS, fixed in 4 % paraformaldehyde, and permeabilized with 0.1 % Triton X-100. Following blocking with 1 % BSA, cells were incubated overnight at 4 °C with the FAP primary antibody (Affinity, China), then treated with the secondary antibody at room temperature for 1 h. DAPI staining was applied for 25 min, and cells were visualized under a fluorescent inverted microscope.

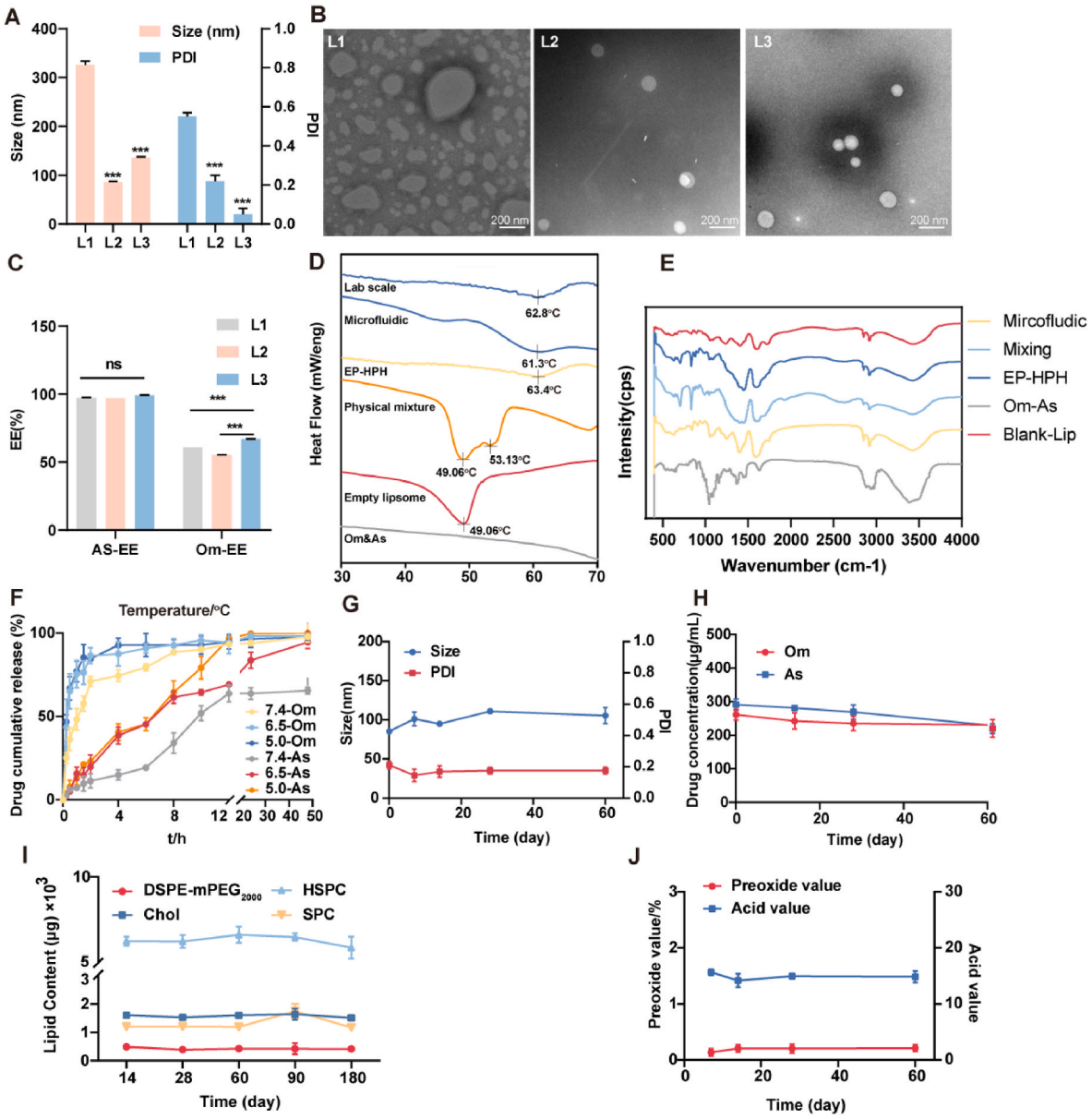

Fig. 3. Characterization, release profile, and stability of liposomes. (A) DLS analysis showing particle size and PDI variations among liposomes prepared without the HPH step (L1), by EP-HPH method (L2), and by microfluidic method (L3) ($n = 3$). (B) TEM images of L1, L2, and L3 (scale bar = 200 nm). (C) As-EE (%) and Om-EE (%) of liposomes ($n = 3$). (D) DSC analysis comparing blank liposomes, drugs (Om-As), mixture, and Om-As-Lip. (E) FTIR spectra of liposomes; (F) Drug release profiles of Om-As-Lip at different pH levels ($n = 3$). (G) Particle size and PDI changes of Om-As-Lip over 60 days ($n = 3$). (H) Concentration changes of Om and As in Om-As-Lip over 60 days ($n = 3$). (I) Lipid concentration changes in Om-As-Lip over 60 days ($n = 3$). (J) Peroxide value and acid value changes in Om-As-Lip over 60 days ($n = 3$). (Data are presented as mean ± SD. *$p < 0.05$, **$p < 0.01$, ***$p < 0.001$).

2.10. ELISA assay

IFN-γ and Granzyme B levels in the samples were measured using ELISA Kits (Jianglai Biological, China) according to the manufacturer's instructions.

2.11. Cell bioenergy tests

TILs were isolated using the Pan T Cell Isolation Kit II (Miltenyi Biotec). The oxygen consumption rate (OCR) was assessed in real-time with the Seahorse XFe96 Analyzer (Agilent Technologies). Cells were seeded into XFe 96-well microplates, washed, and incubated in the base medium at 37 °C for 1 h. The Seahorse XF Cell Mito stress test kit was employed to carry out the measurements, following the manufacturer's protocol.

2.12. Statistical analysis

Data analysis was performed using SPSS 20.0,with all results presented as mean ± standard deviation (SD). A Student's t-test was employed to compare differences between two groups, while one-way analysis of variance (ANOVA) followed by Tukey's post hoc test was used for comparisons across multiple groups. A p-value of less than 0.05 was considered statistically significant.

3. Results and discussion

3.1. Preparation of Om-As-Lip in lab scale and scale-up process optimization

3.1.1. Preparation of liposomes in lab scale

To optimize the scale-up process of Om-As-Lip, the preparation method and formulation were refined at the lab scale. Key factors such as preparation techniques and lipid types were systematically screened. As, a cycloartane-type triterpenoid glycoside, has poor solubility, which limits its encapsulation efficiency (EE) in liposomes [23,31]. In contrast, Om, a highly hydrophilic drug with a low log partition coefficient (log P), is weakly alkaline and struggles to cross the lipid membrane, making its loading into the aqueous core of liposomes challenging [8,9]. Typically, liposomes encapsulating drugs with different polarities are prepared using distinct methods. For hydrophobic drugs, techniques like membrane dispersion or ethanol injection are commonly employed [32], while pH gradient and ammonium sulfate gradient methods are more suitable for hydrophilic drugs. Given the polarity differences between As and Om, separate methods were used to prepare As-Lip and Om-Lip. The ethanol injection method resulted in a higher EE of As (67.54 %) compared to thin film dispersion using various solvents (chloroform: 10.43 %, methanol: chloroform (3:1, v/v): 15.22 %, ethanol: 44.77 %) (Figure S1 A), indicating its suitability for As-Lip preparation. Meanwhile, the pH gradient method demonstrated a superior EE for Om (82.99 %) compared to passive-loading (22.12 %) and the ammonium sulfate gradient method (21.02 %) (Figure S1 B), confirming its appropriateness for Om-Lip preparation.

Based on these findings, a combined ethanol injection and pH gradient method was employed for Om-As-Lip preparation. In this process, As and Om were sequentially loaded into the liposomes. First, As-Lip was formed *via* the ethanol injection method in an acidic environment provided by citric acid solution. The interior of As-Lip remained acidic while the external pH was adjusted to 7.0 by incubating with Na_2CO_3 solution, which created an alkaline environment to keep Om, a weak base, in its uncharged form. During incubation, uncharged Om molecules diffused into the acidic liposomal core, where they became charged [33]. Once charged, Om could no longer pass through the bilayer membrane, thus becoming trapped inside the liposomes [34].

After establishing this combined method, lipid species were further optimized to enhance the EE of both Om and As. Natural lipids like SPC and EPC, with unsaturated acyl chains, improve the EE of hydrophobic drugs by increasing the flexibility of the carbon chains [35]. Conversely, synthetic lipids such as HSPC, with a high melting temperature (T_m) and rigid saturated fatty acid chains, enhance the EE of hydrophilic drugs [35]. Therefore, EPC, SPC, and HSPC were tested for Om-As-Lip preparation. As shown in Figure S1 C and D, SPC resulted in a high EE for As (98.04 %) but a low EE for Om (9.67 %), while HSPC achieved the highest EE for Om (71.13 %) but lower EE for As (58.90 %). After a comprehensive evaluation, a combination of SPC and HSPC was selected for Om-As-Lip preparation *via* the ethanol injection-pH gradient method, yielding an EE of 97.28 ± 0.40 % for As and 60.76 ± 0.01 % for Om. Ultimately, the mixed-lipid formulation maintained high EE values for both Om and As, demonstrating the effectiveness of the combined method.

3.1.2. Scale-up process optimization

Following the successful lab-scale preparation of Om-As-Lip, the scaling-up process was investigated using both the conventional EP-HPH method and a novel microfluidic technique. Typically, liposomes undergo EP-HPH to achieve the desired size and PDI [28]. The schematic of the conventional EP-HPH process is presented in Fig. 2A, where HPH steps were performed after lab-scale preparation (ethanol injection-pH gradient method) to produce unilamellar liposomes, with parameters set at 600 bar for 6 cycles at 4 °C.

Microfluidic technology, on the other hand, offers a rapid and scalable alternative for producing liposomes [36]. The schematic of the novel microfluidic process for Om-As-Lip is shown in Fig. 2B. This method involves two key steps: first, lipid and citric acid aqueous phases are pumped through a mixing chip to form As-Lip; second, after collection, As-Lip is combined with Na_2CO_3 solution (containing Om) *via* two pumps to facilitate the active loading of Om, forming Om-As-Lip.

The critical parameters affecting microfluidic liposome production include flow rate ratio (FRR), total flow rate (TFR), and total volume (TV) [35]. To optimize these parameters for pre-forming As-Lip, the results in Fig. 2C show that increasing FRR and TFR led to smaller liposome particle sizes and improved EE% of As, likely due to enhanced mixing at higher flow rates. Further investigation by increasing the TV showed that liposome size remained stable within the range of 117.0 nm–149.0 nm, with As-EE% remaining high (81.28 %–96.22 %). Among the conditions tested, As-Lip produced with FRRs of 1:4, 1:5, and 1:6 displayed optimal size, low PDI, and high As-EE, making them suitable for subsequent Om loading. Supplementary Fig. 2 indicated that liposomes with an FRR of 1:5 achieved the highest Om-EE%. Therefore, As-Lip prepared at a TFR of 16 mL/min, TV of 12 mL, and FRR of 1:5 was selected for further optimization of Om loading.

Next, we investigated the optimal conditions for the active loading of Om into As-Lip (Fig. 2D). Results indicated that Om-As-Lip prepared with an FRR of 1:2.5 and a TFR of 10 mL/min achieved the highest Om-EE% alongside a desirable particle size. Interestingly, increasing the TV led to further reductions in particle size and improvements in Om-EE%. Consequently, the optimal parameters for Om-As-Lip preparation *via* microfluidics were determined as an FRR of 1:2.5, TFR of 10 mL/min, and TV of 14 mL.

A comparison of scale-up processes between EP-HPH and microfluidic methods demonstrated a significantly higher production rate for the microfluidic approach (21.22 mL/min) compared to EP-HPH (1.19 mL/min). The findings suggest that microfluidics offers a more efficient pathway for industrial-scale production. Additionally, factors such as high-speed shear, vibration, and convective impact in the EP-HPH process may compromise the reproducibility of Om-As-Lip. In contrast, microfluidic technology allows for precise control over critical parameters (FRR, TFR, TV), minimizing batch variability and enhancing consistency. Overall, microfluidics presents considerable potential for scaling up the production of Om-As-Lip in industrial applications.

3.2. Characterization of the liposomes

The physicochemical properties of Om-As-Lip prepared by lab-scale, EP-HPH, and microfluidic processes were thoroughly characterized. Particle size and PDI, measured *via* DLS, are presented in Fig. 3A. The data show that Om-As-Lip produced by the microfluidic method (size: 136.3 ± 1.42 nm, PDI: 0.05 ± 0.02) closely resembled that prepared at the lab scale (size: 134.6 ± 6.2 nm, PDI: 0.20 ± 0.03). However, the coarse emulsion prior to the HPH step exhibited significantly larger particle size and PDI (size: 326.5 ± 7.0 nm, PDI: 0.551 ± 0.021), which were brought back to the desired range following the HPH step (size: 86.61 ± 1.11 nm, PDI: 0.22 ± 0.03). This change is likely due to insufficient energy to overcome lipid aggregation during bulk mixing, a challenge that is addressed by the HPH step [37].

TEM images supported the DLS results (Fig. 3B), revealing that pre-HPH Om-As-Lip exhibited irregular morphology and inconsistent particle sizes, while post-HPH samples displayed a uniform, spherical structure. Similarly, liposomes prepared using the microfluidic method demonstrated consistent spherical shapes.

The EE% for Om and As across the different batches is shown in Fig. 3C. The As-EE% remained consistently high across all methods (lab-scale: 97.28 ± 0.40 %, EP-HPH: 97.05 ± 0.04 %, microfluidic: 99.23 ± 0.02 %). In contrast, significant differences were observed in Om-EE% between the batches (lab-scale: 60.76 ± 0.01 %, EP-HPH: 55.23 ± 1.38 %, microfluidic: 67.01 ± 0.02 %). The reduced Om-EE% in the EP-HPH process could be attributed to the heat generated by strong cavitation

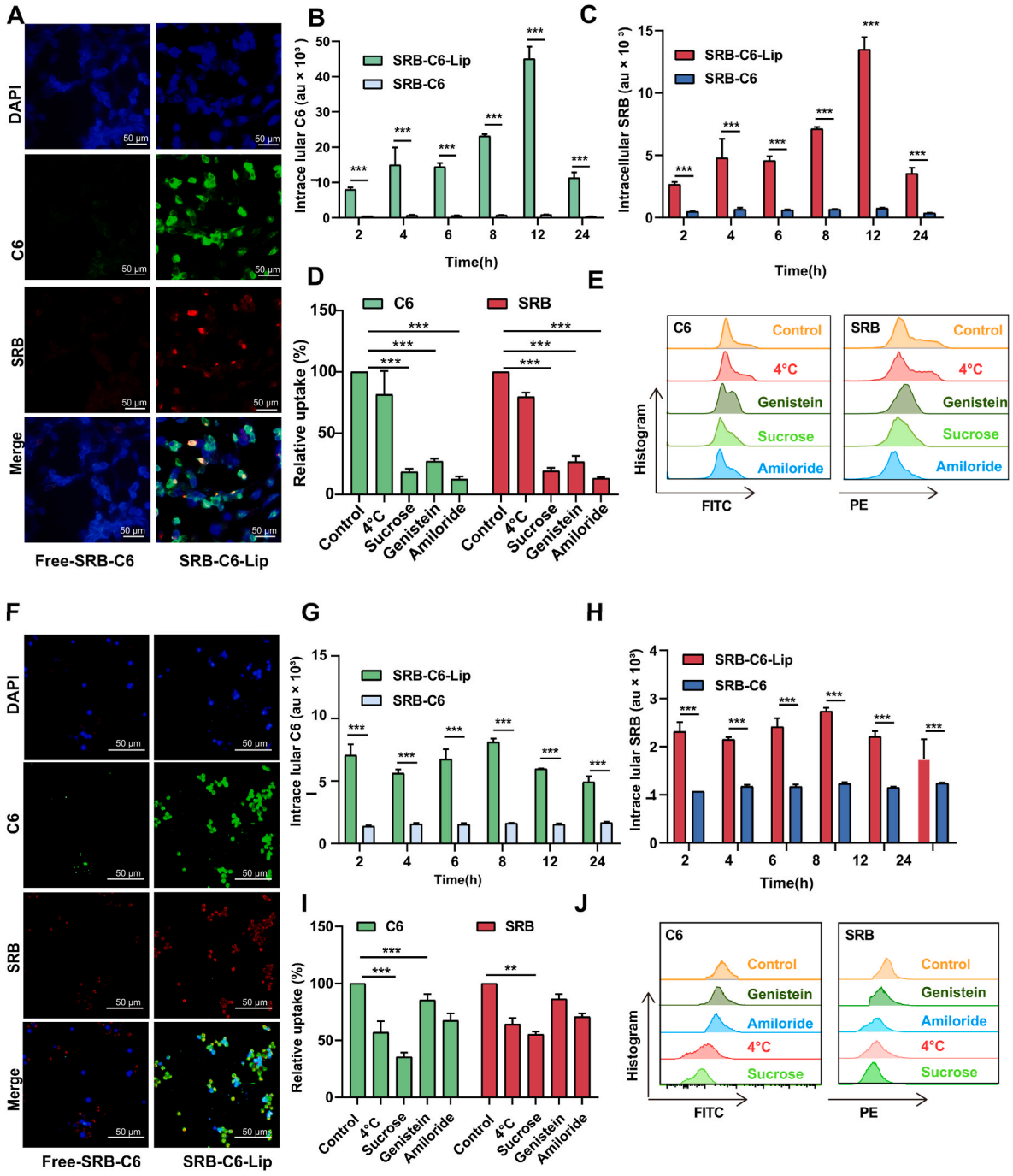

Fig. 4. Cellular uptake of Om-As-Lip. (A) Fluorescence microscopy images showing the uptake of free SRB-C6 and SRB-C6-Lip by CAFs (scale bar = 50 μm); (B) Kinetic profiles of C6 uptake from liposomes by CAFs ($n = 3$); (C) Kinetic profiles of SRB uptake from liposomes by CAFs ($n = 3$); (D, E) Mechanistic analysis of C6 and SRB uptake from SRB-C6-Lip by CAFs ($n = 3$); (F) Fluorescence microscopy images showing the uptake of free SRB-C6 and SRB-C6-Lip by CTLL-2 cells (scale bar = 50 μm); (G) Kinetic profiles of C6 uptake from liposomes by CTLL-2 cells ($n = 3$); (H) Kinetic profiles of SRB uptake from liposomes by CTLL-2 cells ($n = 3$); (I, j) Mechanistic analysis of C6 and SRB uptake from SRB-C6-Lip by CTLL-2 cells ($n = 3$). (Data are presented as mean ± SD, with statistical significance indicated by $^{*}p < 0.05$, $^{**}p < 0.01$, $^{***}p < 0.001$; one-way ANOVA).

and shear forces during homogenization, while the higher Om-EE% in the microfluidic method likely stems from more efficient chaotic advection mixing. CLSM imaging (Fig. S3) further confirmed the successful co-encapsulation of hydrophilic and lipophilic drugs in liposomes prepared by the microfluidic process. Fluorescent dyes, SRB (red fluorescence) and C6 (green fluorescence), were used to label Om and As, respectively, and the overlapping yellow signals indicated effective dual-drug encapsulation.

DSC analysis (Fig. 3D) was employed to examine the phase transition behavior of the liposomes. The calorimetric profiles revealed that the phase transition temperature (T_m) of Om-As-Lip across different batches (lab-scale: 60.2 °C, EP-HPH: 61.03 °C, microfluidic: 63.4 °C) was higher than that of blank liposomes (49.06 °C), suggesting improved thermal stability for Om-As-Lip below T_m, which enhances its potential stability.

Infrared spectroscopy was subsequently employed to further investigate molecular interactions within the liposomes. Changes in molecular arrangement due to these interactions manifest as shifts in the absorption peaks of specific functional groups. The FTIR spectra of the

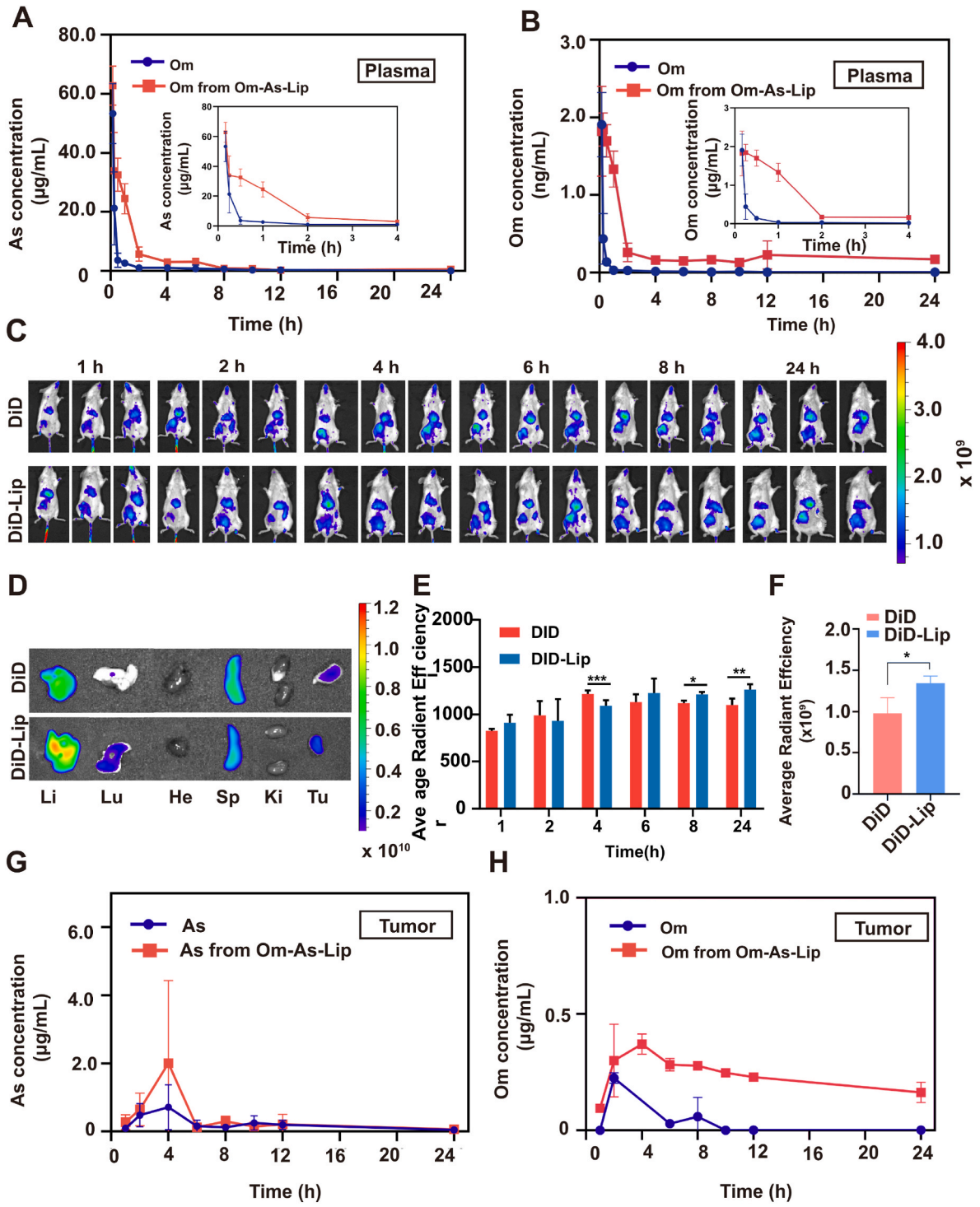

Fig. 5. Biodistribution of Om-As-Lip. (A) Concentration-time curve of As from Om-As-Lip and free Om-As in 4T1 tumor-bearing mice ($n = 6$). (B) Concentration-time curve of Om from Om-As-Lip and free Om-As in 4T1 tumor-bearing mice ($n = 6$). (C) IVIS Spectrum imaging visualizing the distribution of free DiD and DiD-Lip in 4T1 tumor-bearing mice. (D) *Ex vivo* imaging of various organs and tumor tissues 24 h post-injection, captured using the IVIS Spectrum. (E) Quantitative analysis of fluorescence intensity in tumor tissues at different time points ($n = 3$). (F) Quantitative analysis of fluorescence intensity in isolated tumor tissues ($n = 3$). (G) Mean drug concentration of As in tumor tissues from Om-As-Lip and free Om-As ($n = 6$). (H) Mean drug concentration of Om in tumor tissues from Om-As-Lip and free Om-As ($n = 6$). (Data are presented as mean ± SD, with statistical significance compared to the free drugs group (DiD, Om, As): $^*p < 0.05$, $^{**}p < 0.01$, $^{***}p < 0.001$.).

liposomes (lab scale, EP-HPH, and microfluidic) are presented in Fig. 3E. In the FTIR spectrum of Om-As, the absorption peak at 1609 cm^{-1} corresponds to the C=O stretching vibration, while the band at 947 cm^{-1} is attributed to the N-O group. Notably, the N-O vibration peak of Om disappeared in the FTIR spectrum of the liposomes, indicating successful encapsulation of Om. Additionally, the C-O stretching vibration peak of the empty liposomes, typically found at 1236 cm^{-1}, shifted to 1253 cm^{-1} in Om-As-Lip, likely due to the formation of hydroxyl groups from As. The emergence of hydrogen bonding may facilitate the high dispersion of As within the lipid layer.

The viscosity of the liposomes was also measured, revealing low viscosity across all three preparation methods, making them suitable for

Table 1
Pharmacokinetic parameters of Om-As-Lip, free Om, and As in plasma and tumor.

	Pharmacokinetic parameters	Free Om	Free As	As from (Om-As-Lip)	Om from (Om-As-Lip)
Plasma	C_{max} (μg/L)	1.75 ± 0.31	52.22 ± 9.04	63.58 ± 4.99$^{\#}$	2.06 ± 0.45
	T_{max} (h)	0.17 ± 0.01	0.17 ± 0.01	0.18 ± 0.03	0.29 ± 0.16**
	AUC (μg/L h)	1.01 ± 0.25	38.77 ± 12.39	79.02 ± 5.98$^{\#\#\#}$	6.24 ± 2.45***
	$t_{1/2}$ (h)	5.66 ± 2.12	1.73 ± 1.03	3.25 ± 1.58$^{\#\#\#}$	19.34 ± 1.43***
	MRT (h)	2.12 ± 1.19	1.73 ± 0.50	3.07 ± 1.17$^{\#}$	6.61 ± 3.09*
Tumor	C_{max} (μg/L)	0.92 ± 0.43	0.64 ± 0.26	2.67 ± 2.29$^{\#\#\#}$	1.41 ± 0.60
	AUC (μg/L h)	6.09 ± 3.96	6.04 ± 2.43	15.27 ± 10.12	18.44 ± 7.10
	MRT (h)	6.95 ± 2.83	5.36 ± 2.05	5.96 ± 1.18	10.53 ± 0.81

[a]Cmax, maximum plasma concentration; T_{max}, time of maximum concentration; AUC (μg/L h), are under the curve from time 0–24 h; $t_{1/2}$ (h), half-life at the bio-distribution phase; MRT (h), time of drug residence in the plasma and tumor. ($n = 6$, $^{*}P < 0.5$, $^{**}P < 0.1$, $^{***}P < 0.01$, compared to free Om, $^{\#}p < 0.5$, $^{\#\#}p < 0.1$, $^{\#\#\#}p < 0.01$, compared to free As. All data are presented as mean ± SD).

injection (lab batch: 1.64 ± 0.02 mPa s, EP-HPH: 3.43 ± 0.05 mPa S, microfluidic: 25.46 ± 0.41 mPa S) [38]. Furthermore, the pH values of the liposomes prepared by all three methods were within the range suitable for intravenous administration (lab batch: 6.72 ± 0.09, EP-HPH: 6.68 ± 0.13, microfluidic: 6.74 ± 0.20).

Given these findings, Om-As-Lip produced *via* the microfluidic method demonstrated high drug entrapment efficiency and holds significant potential for further development. This method was therefore selected for subsequent studies involving Om-As-Lip.

3.3. Release profile of the liposomes prepared by microfluidic

The drug release profiles of Om-As-Lip were evaluated in various acidic environments (Fig. 3F). As the pH decreased from 7.4 to 5.0, an increase in the release rate of Om-As-Lip was observed. At pH 6.5, the cumulative release of Om increased by 13 %, and at pH 5.0, it increased by 20 % within 4 h, compared to pH 7.4. Similarly, the cumulative release of As rose by 25 % at pH 6.5 and by 36 % at pH 5.0 over 24 h. The drug release of Om-As-Lip in response to the acidic tumor microenvironment may be due to the conformational change of the DSPE-$mPEG_{2000}$ polymer in the formulation under acidic conditions, leading to the disintegration of the liposomes and subsequent drug release. These results suggest that Om-As-Lip releases its drugs more effectively in the acidic tumor microenvironment, making it a responsive drug delivery system.

3.4. Stability of the liposomes prepared by microfluidic

The stability of liposomes is critical for their practical applications [39]. The physical stability of Om-As-Lip was assessed by monitoring particle size, PDI, and the content of Om, As, and lipid components (HSPC, SPC, cholesterol, and DSPE-$mPEG_{2000}$) over 60 days. The results revealed that both the particle size and PDI of Om-As-Lip remained consistent throughout the observation period (Fig. 3G). Additionally, the content of Om, As, and lipid components showed no significant changes over time (Fig. 3H and I). These data indicate that Om-As-Lip can be stably stored at 4 °C for at least two months.

Lipids are prone to degradation through oxidation of poly-unsaturated hydrocarbon chains and ester hydrolysis, which produce oxidized lysophosphatidic and free fatty acid derivatives [40]. These degradation products can affect the chemical stability of liposomes. To assess this, the PV and acid values were measured over 60 days [30]. According to regulatory standards, the PV should be below 3.0 and the acid value below 15. The PV and acid values of Om-As-Lip were found to be 0.20 and 14 (Fig. 3J), respectively, both within the acceptable range, indicating high chemical stability. The primary factor contributing to this stability is the high concentration of HSPC, which enhances inter-molecular forces and forms a tighter lipid structure, thus preventing lipid oxidation and reducing the production of fatty acid derivatives.

Overall, these results underscore the successful preparation of Om-As-Lip, characterized by excellent physical and chemical stability, making it a promising candidate for further development.

3.5. Cells uptake

To explore the cellular uptake of Om-As-Lip prepared *via* microfluidics, hydrophilic fluorescent dye SRB and hydrophobic C6 were substituted for Om and As [41]. Fluorescence microscopy and flow cytometry were utilized to visualize the uptake of SRB-C6-Lip by CAFs and CTLL-2 cells [42]. Fig. 4A and B, and C shows that the uptake of C6 (green) and SRB (red) by CAFs from SRB-C6-Lip reached peak mean fluorescence intensities (MFI) of 40 k and 12 k, respectively, after 12 h. The uptake rate of C6 and SRB from SRB-C6-Lip was 53-fold and 18-fold higher ($P < 0.001$), respectively, compared to free C6-SRB. A same trend was observed in CTLL-2 cells, where the peak MFI for C6 and SRB reached 8 k and 2.6 k, respectively, after 8 h. The uptake rate of C6 and SRB by CTLL-2 cells was 4.99-fold and 2.22-fold higher ($P < 0.001$), respectively, compared to free SRB-C6 (Fig. 4F, G, H). These results indicate that Om-As-Lip significantly enhances the uptake of Om-As by both CAFs and CTLL-2 cells.

The mechanism underlying Om-As-Lip uptake was further investigated. Endocytosis was inhibited at 4 °C to assess energy dependence, while sucrose, genistein, and amiloride were employed to inhibit clathrin-mediated, caveolae-mediated, and pinocytosis pathways, respectively [12]. As shown in Fig. 4D, E, I, and J, CAFs and CTLL-2 cells endocytosed SRB-C6-Lips *via* multiple pathways, including pinocytosis and both the clathrin- and caveolae-mediated endocytosis. Additionally, CTLL-2 cells demonstrated energy-dependent uptake of SRB-C6-Lips.

3.6. In vivo pharmacokinetics and biodistribution

The pharmacokinetics of Om-As-Lip were evaluated in orthotopic 4T1 tumor-bearing mice (Fig. 5A and B, and S4; Tables S4–S8). Drug PK parameters, calculated using a non-compartmental model, are presented in Table 1. Co-loading Om and As in the liposomes significantly increased the plasma AUC of both drugs compared to their free-drug forms (3.42-fold for Om and 2.03-fold for As), indicating that Om-As-Lip enhanced the bioavailability of both agents. Plasma C_{max} values for Om and As increased 1.16-fold and 1.22-fold, respectively, in the Om-As-Lip formulation compared to the free drug solution, demonstrating that the liposomes effectively elevated drug concentrations in the plasma. Additionally, co-loading Om and As in liposomes extended the plasma half-life (6.17-fold for Om, 1.88-fold for As) and MRT (3.11-fold for Om, 1.77-fold for As), indicating prolonged *in vivo* circulation and reduced clearance rates compared to the free drug.

Fig. 5G–H displays the distribution of Om-As-Lip and free Om-As in tumors. The data revealed a marked increase in tumor AUC for both drugs in the Om-As-Lip formulation compared to the free drugs (4.19-fold for Om, 2.0-fold for As). Similarly, C_{max} values increased by 1.58-fold for Om and 3.49-fold for As, indicating significantly higher drug concentrations in the tumor tissue. The peak concentration of both drugs was reached at approximately 2.6 h for Om and 4.03 h for As post-

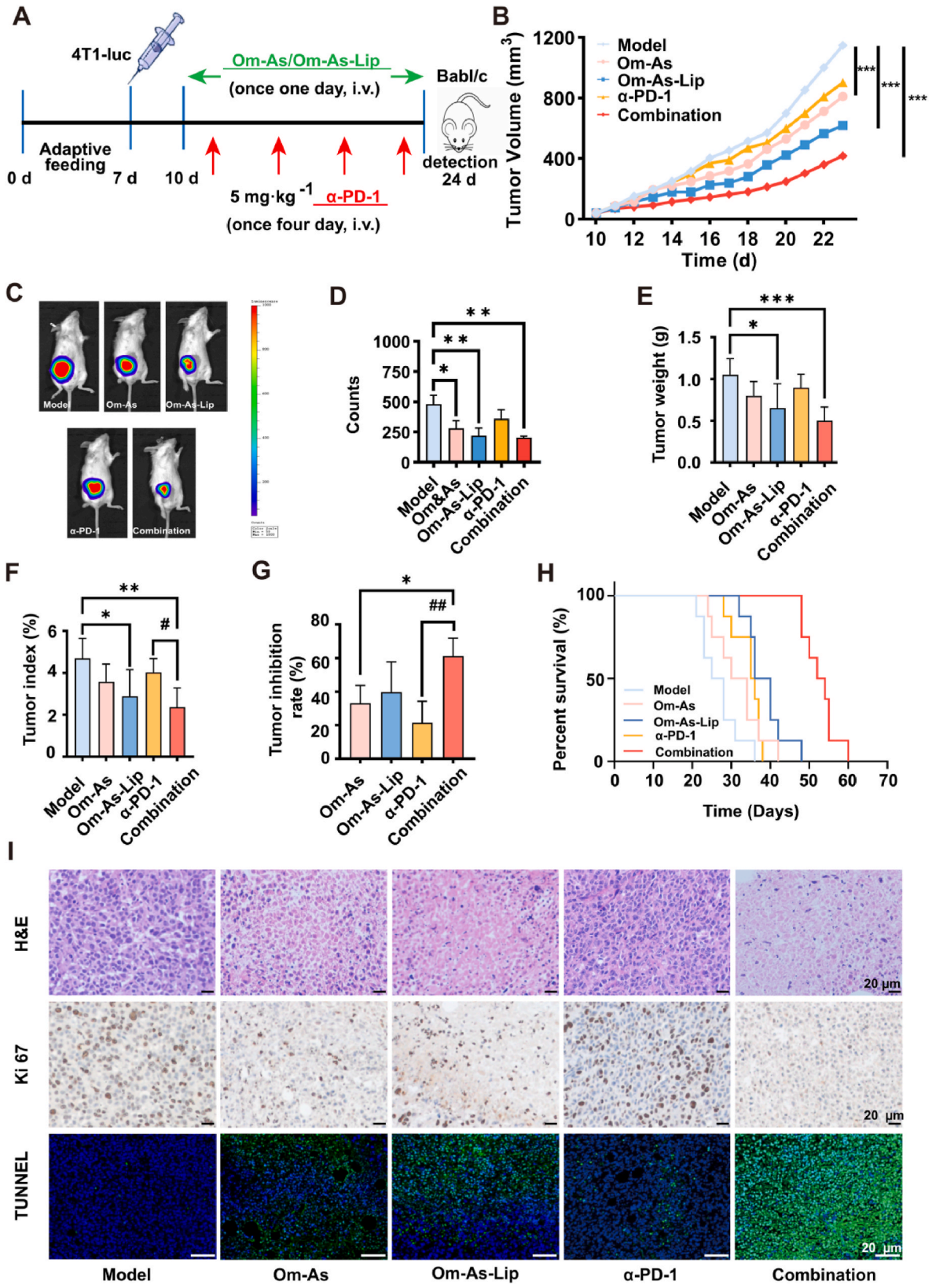

Fig. 6. Antitumor therapeutic effect of Om-As-Lip *in vivo*. (A) Schematic representation of the treatment regimen. (B) Tumor volume changes in 4T1-Luc tumor-bearing mice across different treatment groups ($n = 6$). (C, D) Bioluminescent imaging illustrating tumor activity *in vivo*. (E) Tumor weight in each group after treatment ($n = 6$). (F) Tumor index of 4T1-Luc tumor-bearing mice post-treatment ($n = 6$). (G) Tumor suppression rates in different groups ($n = 6$). (H) Survival curves of the mice in each group ($n = 8$). (I) H&E staining, Ki67 IHC staining, and TUNEL IF staining of tumors from different groups (scale bars = 100 μm). (Data are presented as mean ± SD; $^{*}p < 0.05$, $^{**}p < 0.01$, $^{***}p < 0.001$; one-way ANOVA).

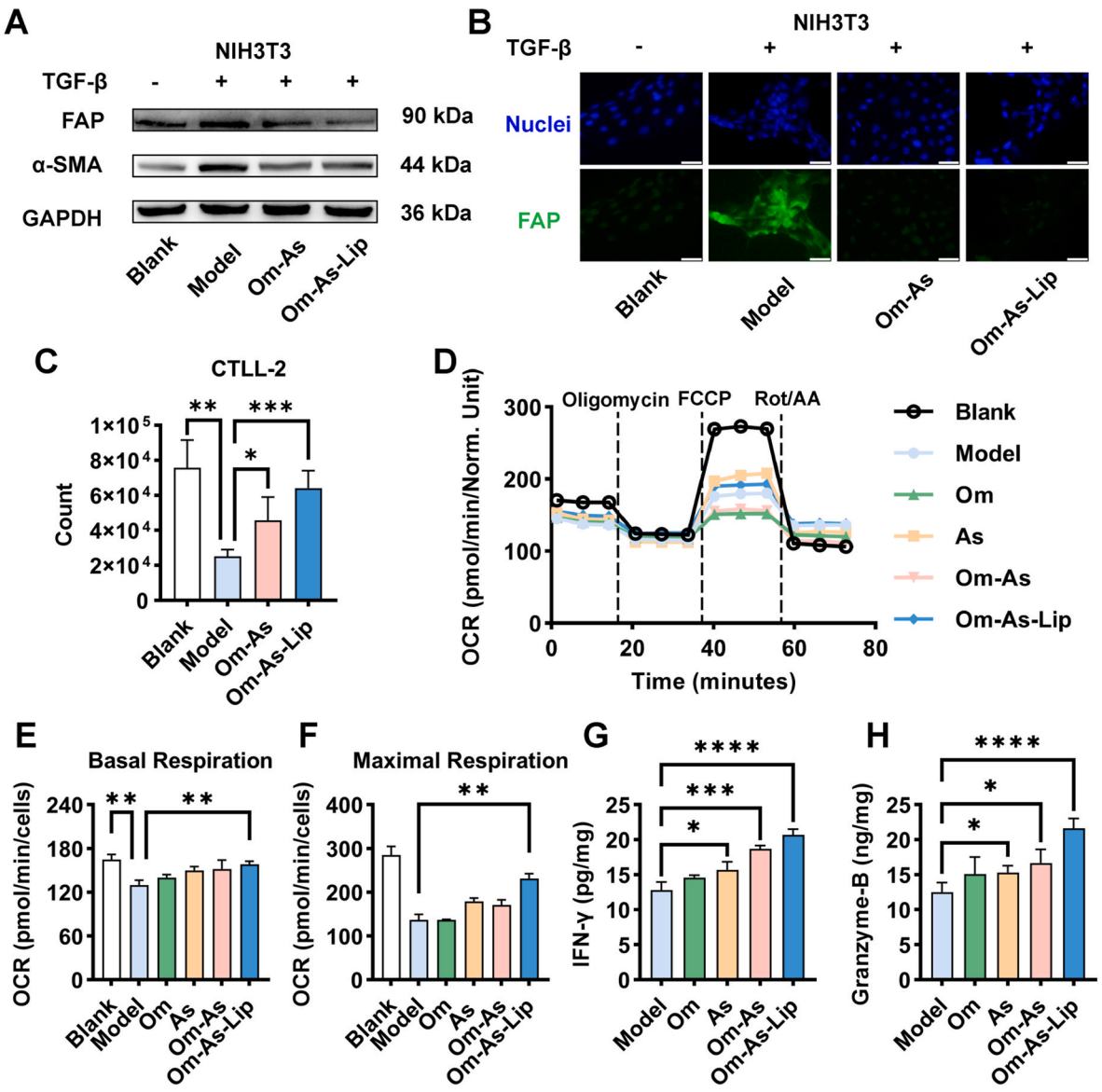

Fig. 7. Inhibition of CAFs and enhancement of TIL mitochondrial function by Om-As-Lip. (A) Western blot analysis showing the effect of Om-As-Lip on the expression of the CAF marker α-SMA. (B) Cellular immunofluorescence assay displaying the effect of Om-As-Lip on FAP expression in CAFs (scale bar = 50 μm). (C) Flow cytometry analysis of the number of CTLL-2 cells infiltrating through CAFs following treatment with different concentrations of Om-As-Lip (n = 6). (D) Basal respiration measured by OCR before and after oligomycin addition (n = 3). (E) OCR measurements before and after Rot/AA injection (n = 3). (F) Maximum respiratory capacity determined by OCR after FCCP injection (n = 3). (G) Quantification of IFN-γ (H) and Granzyme B by ELISA in T cells cocultured with tumor cells (n = 4). (Data are shown as mean ± SD. $^*P < 0.05$, $^{**}P < 0.01$, $^{***}P < 0.001$; one-way ANOVA).

injection for all formulations. The MRT of both drugs was also substantially prolonged in tumor tissue with liposomal delivery, demonstrating the ability of liposomes to prevent rapid clearance and enhance drug accumulation in tumors.

To visualize *in vivo* liposome distribution, DiD-Lip was administered *via* tail vein injection to Balb/c mice bearing 4T1 tumors, and fluorescence imaging was performed using a small animal imaging system. As shown in Fig. 5C, D, a strong fluorescence signal was detected at the tumor site in mice treated with DiD-Lip (1.383 ± 0.15, a.u.), indicating superior tumor accumulation compared to mice treated with free DiD. At 24 h post-injection, *ex vivo* fluorescence imaging of the tumors confirmed stronger fluorescence in the DiD-Lip group (Fig. 5E and F), further supporting the role of liposomes in enhancing drug accumulation at the tumor site.

Overall, the data demonstrate the advantages of co-loading drugs into liposomes, which improve treatment efficacy by enhancing tumor targeting and retention of Om-As.

3.7. *In vivo anti-tumor efficacy of Om-As-Lip in combination with α-PD-1*

The antitumor efficacy of the combination of Om-As-Lip and α-PD-1 therapy was evaluated in orthotopic 4T1 tumor-bearing mice (Fig. 6A). Tumor volume was measured daily throughout the treatment period. The results indicated that Om-As-Lip significantly inhibited tumor growth compared to the model group, and tumor growth was further suppressed when combined with α-PD-1 therapy (Fig. 6B). At the conclusion of the 14-day treatment, *in vivo* bioluminescence imaging revealed that the fluorescence intensity in the Om-As-Lip group was markedly reduced compared to the model group, with the lowest fluorescence observed in the combination group (Fig. 6C and D).

Following treatment, the mice were euthanized, and the tumors were excised for analysis (Fig. S5). Tumor volume, tumor weight, tumor index, and tumor suppression rates were assessed (Fig. 6E–G). Tumor weight significantly decreased in the Om-As-Lip group compared to the model group, especially in the combination treatment group. Both the

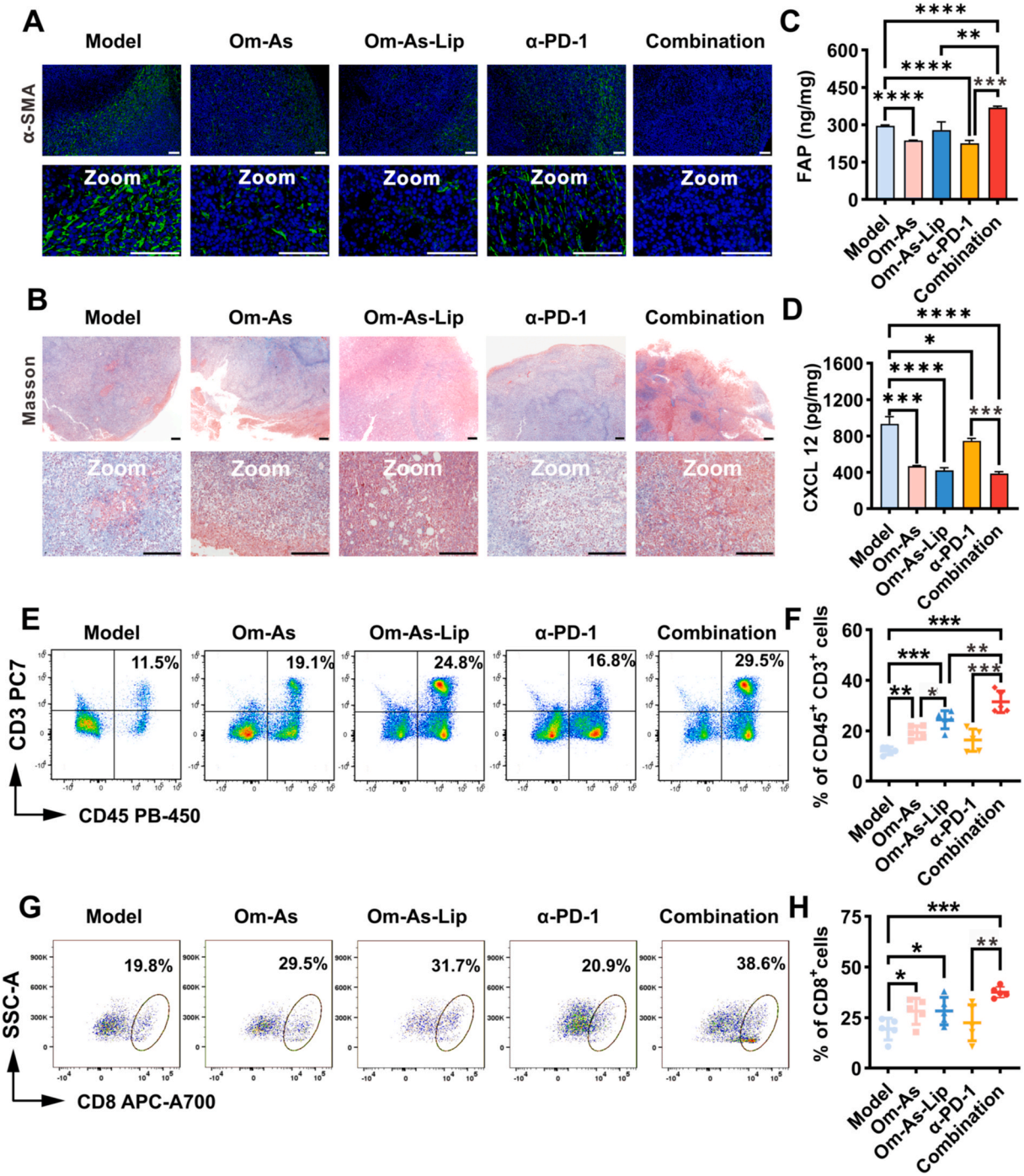

Fig. 8. Om-As-Lip Upregulates the Expression of TILs by Inhibiting CAFs *in vivo*. (A) Representative α-SMA staining results for 4T1-Luc tumors in each treatment group (scale bars = 200 μm). (B) Representative Masson staining results for 4T1-Luc tumors in each treatment group (scale bars = 200 μm). (C) Quantification of FAP (D) and CXCL12 levels in 4T1-Luc tumors as measured by ELISA ($n = 4$). (E) Flow cytometry analysis of $CD45^{+}$T $CD3^{+}$T cells in 4T1-Luc tumors (F) and quantitative analysis ($n = 5$). (G) Flow cytometry analysis of $CD8^{+}$T cells in 4T1-Luc tumors (H) and quantitative analysis ($n = 5$). (Data are presented as mean ± SD; $^{*}P < 0.05$, $^{**}P < 0.01$, $^{***}P < 0.001$; one-way ANOVA).

Om-As-Lip and combination groups showed a reduction in tumor indices compared to the model group, with the combination group displaying a significantly lower tumor index than the α-PD-1 group. Tumor inhibition rates were 39.75 % for Om-As-Lip, 21.43 % for α-PD-1, and 61.20 % for the combination therapy. The combination group demonstrated a 2.67-fold increase in tumor inhibition rate compared to α-PD-1 alone, indicating that Om-As-Lip significantly enhances the antitumor efficacy of α-PD-1. Additionally, the median survival time in the combination group extended to 46 days (Fig. 7H), surpassing that of the model group (27 days), the Om-As group (36 days), and the Om-As-Lip group (40 days). This suggests that the combination of Om-As-Lip and α-PD-1 not only inhibits tumor growth but also prolongs survival in the treated animals.

Histological analysis using H&E staining, Ki67 immunohistochemistry, and TUNEL immunofluorescence was conducted to further evaluate the effects of Om-As-Lip combined with α-PD-1 on tumor suppression (Fig. 7I). In comparison to the model group, the Om-As, Om-As-Lip, and combination groups exhibited significant tumor necrosis, with the largest necrotic area observed in the combination groups group.

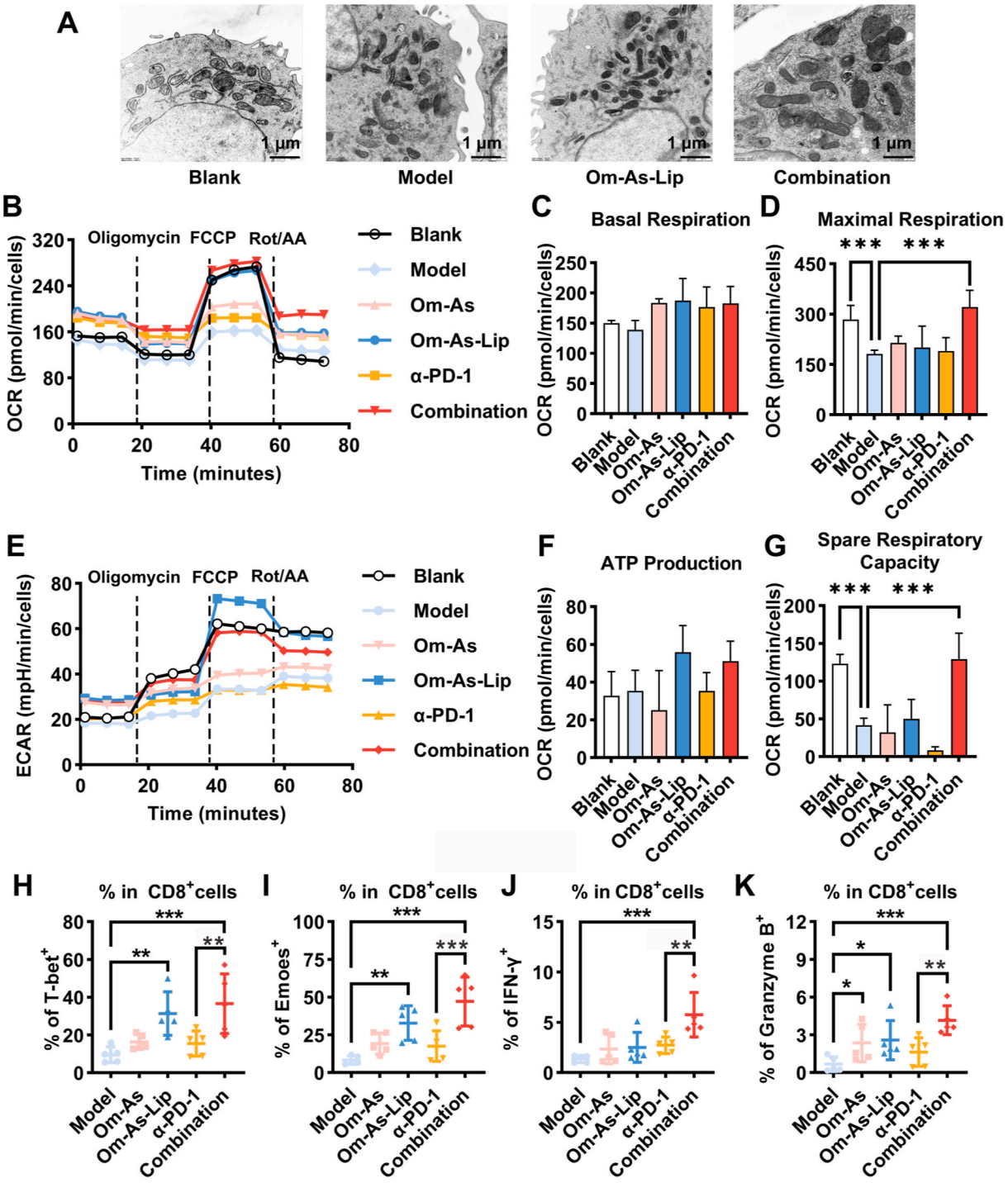

Fig. 9. Om-As-Lip enhances $CD8^+$TIL activity by improving mitochondrial function *in vivo*. (A) TEM images of TIL mitochondria (scale bar = 1 μm). (B) Basal respiration ($n = 4$). (C) OCR measured before oligomycin addition and after Rot/AA injection ($n = 4$). (D) Maximal respiratory capacity ($n = 4$). (E) ECR changes indicating maximal mitochondrial activity ($n = 4$). (F) ATP production measured as the decrease in OCR following oligomycin addition ($n = 4$). (G)Spare respiratory capacity, the gap between cellular respiration and the theoretical maximum ($n = 4$). (H) Flow cytometry analysis of $CD8^+$ TILs showing the proportion of T-bet^+, (I) $Eomes^+$, (J) IFN-γ^+, (K) and Granzyme B^+ ($n = 5$). (Data are presented as mean ± SD; $^*P < 0.05$, $^{**}P < 0.01$, $^{***}P < 0.001$; one-way ANOVA).

The Ki67-positive areas, indicative of proliferation, were reduced in all treatment groups, particularly in the combination group. TUNEL immunofluorescence further confirmed that the Om-As-Lip and combination groups induced a higher rate of apoptosis.

In summary, consistent with existing literature, α-PD-1 alone exhibits a low response rate in breast cancer [43]. However, Om-As-Lip enhances the antitumor efficacy of Om-As by improving its bioavailability. When combined with α-PD-1, it further enhances therapeutic outcomes.

3.8. *Inhibition of CAF activity and enhanced mitochondrial function in TIL in vitro by Om-As-Lip*

The antitumor efficacy of PD-1 inhibitors is strongly associated with the infiltration and activity of TILs [44]. In breast cancer, the presence of CAFs and impaired mitochondrial function in TILs result in low

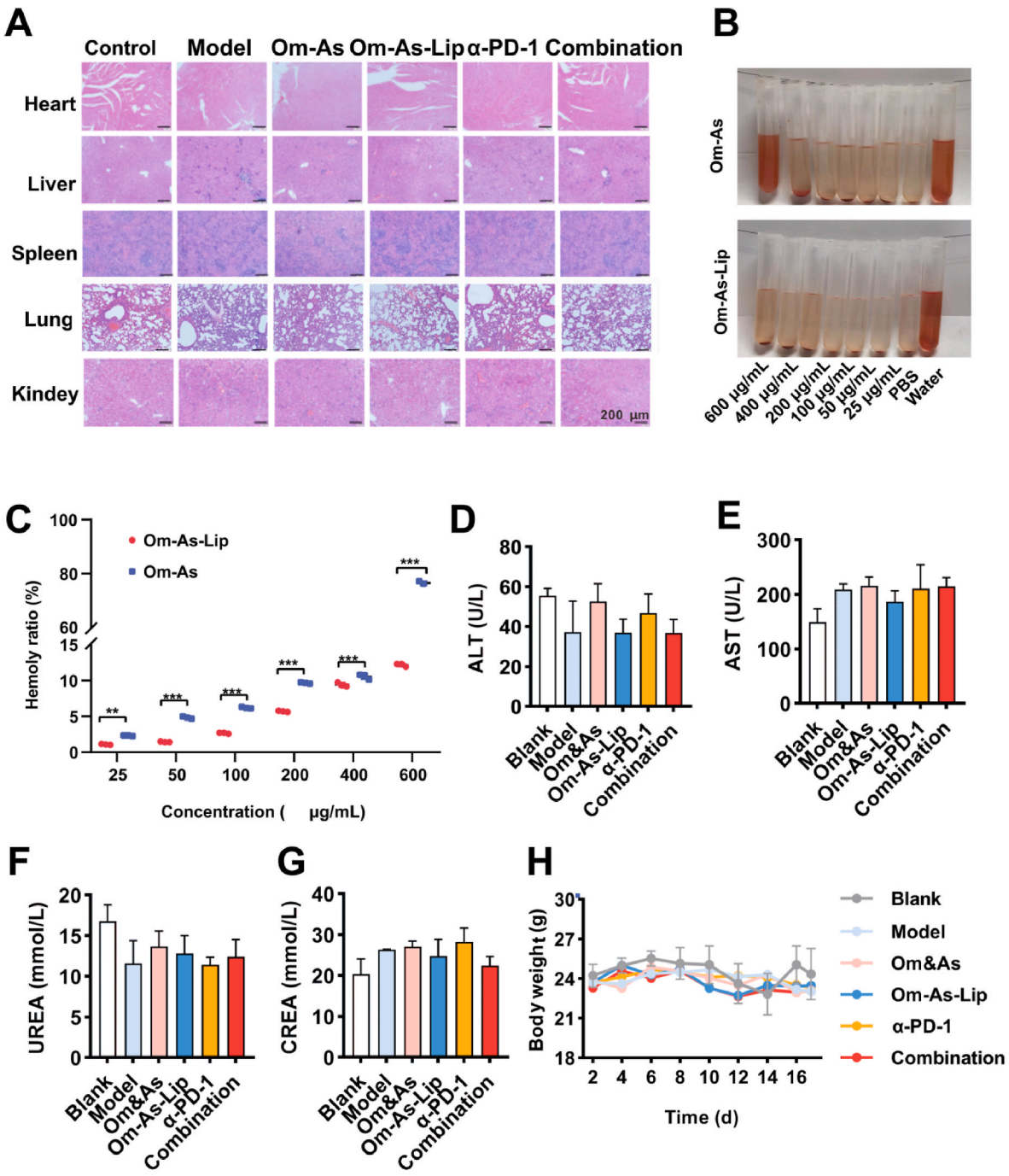

Fig. 10. Safety evaluation of Om-As-Lip. (A) H&E staining of major organs in mice after treatment in each group, showing no visible organ damage; (B, C) Hemolytic properties of Om-As and Om-As-Lip tested and statistically analyzed ($n = 6$). (D) ALT, (E) AST, (F) UREA, and (G) CREA levels ($n = 6$). (H) Changes in body weight of mice in each group during the treatment period ($n = 5$). (Data are presented as mean ± SD; $^{*}P < 0.05$, $^{**}P < 0.01$, $^{***}P < 0.001$; one-way ANOVA).

infiltration and poor activity, which ultimately limits the effectiveness of PD-1 inhibitors [45].

Previous studies have demonstrated that Om and As enhance TIL infiltration and activity by inhibiting CAF activation and improving mitochondrial function in TILs [8,12]. In this study, to validate the role of Om-As-Lip in inhibiting CAF activation and promoting TIL infiltration, a CAF model was established by treating NIH3T3 cells with 5 ng/mL TGF-β1 *in vitro*. Activated CAFs typically exhibit increased levels of α-smooth muscle actin (α-SMA) and fibroblast activation protein-α (FAP). The treatment with Om-As-Lip resulted in a significant reduction in the expression of α-SMA and FAP in CAFs (Fig. 7A and B), indicating that Om-As-Lip effectively inhibited CAFs activation. Furthermore, Om-As-Lip treatment substantially enhanced T cell migration across CAFs (Fig. 7C), confirming that CAF deactivation promotes TIL infiltration.

Additionally, TILs require functional mitochondria to generate ATP through respiration for their potent antitumor effects. In breast cancer, mitochondrial dysfunction in TILs reduces their tumor-killing capacity [46]. To assess the impact of Om-As-Lip on mitochondrial function in TILs, a TIL model was simulated by coculturing CTLL-2 cells with 4T1 cells. The oxygen consumption rate (OCR), an indicator of mitochondrial function [47], was measured using the Seahorse XFe96 (Fig. 7D). Results showed that mitochondrial respiration was impaired after T cells were cocultured with tumor cells, while Om-As-Lip treatment

significantly increased oxidative phosphorylation, thereby improving TIL mitochondrial function (Fig. 7E–F). The effect of Om-As-Lip on the antitumor activity of TILs was also evaluated. Activated TILs secrete high levels of IFN-γ and Granzyme B, which induce apoptosis in tumor cells, exerting antitumor effects [48]. ELISA results indicated a significant increase in IFN-γ secretion following Om-As-Lip treatment (Fig. 7G), along with an upregulation of Granzyme B expression (Fig. 7H). In summary, these results suggest that Om-As-Lip enhances TIL antitumor activity by improving mitochondrial function, highlighting its potential for improving the efficacy of PD-1 inhibitor therapies.

3.9. *In vivo inhibition of CAFs by Om-As-Lip upregulated TILs expression*

The mechanism behind the synergistic enhancement of Om-As-Lip in combination with α-PD-1 was further explored *in vivo*. Immunofluorescence staining demonstrated a decreased expression of α-SMA, a key marker of CAF activation, in tumor tissues treated with Om-As-Lip and combination therapy, indicating that Om-As-Lip effectively inhibits CAF activation (Fig. 8A). Activated CAFs are known to suppress TIL expression by secreting collagen, FAP, and CXCL12, which ultimately reduces the efficacy of α-PD-1 [49,50]. Masson staining revealed significant collagen deposition in the model group, whereas both the Om-As-Lip and combination therapy groups exhibited markedly less collagen accumulation in tumor tissues (Fig. 8B), suggesting that Om-As-Lip effectively suppresses collagen secretion by CAFs. ELISA further confirmed that Om-As-Lip and combination therapy significantly decreased FAP and CXCL12 levels in 4T1-luc in situ tumors, with the combination group showing notably lower expression of these markers compared to the α-PD-1 group (Fig. 8C and D).

Flow cytometry analysis was conducted to assess the abundance of TILs in tumor tissues. Results indicated a significant increase in $CD45^+CD3^+$ TILs in the Om-As-Lip group compared to the model group, suggesting that Om-As-Lip enhances overall TIL levels. Additionally, the combination group exhibited significantly higher $CD3^+$ TIL counts than the α-PD-1 group (Fig. 8E and F). $CD8^+$ cytotoxic T lymphocytes (CTLs), the primary immune cells for targeting cancer [48], are often hindered by CAFs, which act as a barrier preventing $CD8^+$ TILs from exerting their antitumor effects [49]. Flow cytometry revealed a notable increase in $CD8^+$ TILs in both the Om-As-Lip and combination groups, with no significant change observed in the α-PD-1 group alone, consistent with existing literature40 (Fig. 8G and H).

In conclusion, these results indicate that Om-As-Lip enhances TIL infiltration by inhibiting CAF activation, thereby improving the antitumor efficacy of the combined Om-As-Lip and α-PD-1 therapy.

3.10. *In vivo enhancement of TILs activity by Om-As-Lip*

Mitochondrial dysfunction impairs the activity of TILs, thereby reducing the antitumor efficacy of α-PD-1 [50,51]. To assess whether Om-As-Lip and combination therapy improved TIL activity by modulating mitochondrial function *in vivo*, TILs were isolated from 4T1-Luc tumors using MACS technology. TEM analysis revealed that mitochondria in the TILs from both the Om-As-Lip group and the combination therapy group were longer and exhibited more cristae (Fig. 9A), indicating enhanced mitochondrial function in these TILs. Further investigation through mitochondrial stress assays confirmed these findings, as basal OCR, ATP production, and maximal respiration of TILs from 4T1-Luc tumors were significantly elevated following Om-As-Lip and combination therapy treatment. Notably, the enhancement in respiratory capacity was more pronounced in the combination group compared to the Om-As-Lip group alone (Fig. 9B–G).

Next, the antitumor activity of $CD8^+$TILs was explored. The T-box transcription factors T-bet and Eomesodermin (Eomes) are critical for the differentiation of effector and memory CTLs and play key roles in preventing $CD8^+$TIL exhaustion [52,53]. Both T-bet and Eomes regulate early and late stages of IFN-γ and granzyme B expression during effector CTL differentiation [54–56]. The present study showed that combination therapy significantly upregulated T-bet and Eomes expression in $CD8^+$TILs (Fig. 9H, I, S6A, B). Correspondingly, the expression of IFN-γ and granzyme B increased, reflecting the activation of $CD8^+$TILs [56,57]. Flow cytometric analysis further demonstrated that the combination of Om-As-Lip and α-PD-1 markedly enhanced the expression of IFN-γ and granzyme B in $CD8^+$TILs, suggesting a substantial improvement in immune function and antitumor activity of these cells in the combined treatment group (Fig. 9J, K, S6C, D).

3.11. *Safety of the combination treatment of Om-As-Lip and α-PD-1*

Tissue sections and organ indices were used to assess the biosafety of the combination therapy involving Om-As-Lip and α-PD-1. Histological analysis revealed no organ damage in any of the treatment groups (Fig. 10A). Hemolysis assay results indicated that As at high concentrations (600 μg/mL) could cause hemolysis, whereas Om-As-Lip did not, suggesting that Om-As-Lip reduces the hemolytic risk associated with As (Fig. 10B and C). Biochemical analyses further demonstrated that the combination therapy of Om-As-Lip and α-PD-1 did not induce hepatotoxicity or nephrotoxicity (Fig. 10D–G). Additionally, body weight measurements showed no significant differences among the groups (Fig. 10H), further supporting the safety profile of the combination therapy. In summary, these results indicate that Om-As-Lip and α-PD-1 combination therapy exhibits a favorable safety profile.

4. Conclusion

In this study, Om-As-Lip was successfully prepared at both laboratory scale and through scale-up processes. The results demonstrated that the microfluidic preparation of Om-As-Lip offers a higher production rate and enhanced stability, making it suitable for industrial transformation. Om-As-Lip efficiently delivered Om and As to tumor tissues in a sustained manner, resulting in prolonged blood circulation and increased bioavailability. The formulation enhanced the antitumor efficacy of α-PD-1 by promoting TILs infiltration and improving their activity, which extended survival time while maintaining a favorable safety profile. In conclusion, this study presents a feasible and scalable approach for industrial production and provides a promising strategy for enhancing the effectiveness of breast cancer immunotherapy in clinical settings.

CRediT authorship contribution statement

Liangyin Wei: Data curation. **Hong Wang:** Data curation. **Xietao Ye:** Formal analysis. **Junfan Yue:** Methodology. **Hong Guo:** Conceptualization. **Dengxuan Mao:** Software. **Xia Li:** Software. **Yeyang Sun:** Validation. **Congyan Liu:** Supervision. **Yuping Liu:** Methodology. **Yan Chen:** Funding acquisition.

Declaration of competing interest

The authors declare no competing financial interest.

Acknowledgement

This work was supported by the National Natural Science Foundation of China (82173985), the Social Development Project of Jiangsu Province (BE2021754), and Jiangsu Province Leading Talents Cultivation Project for Traditional Chinese Medicine (SLJ0318).

Appendix A. Supplementary data

Supplementary data to this article can be found online at https://doi.org/10.1016/j.mtbio.2025.101634.

Data availability

No data was used for the research described in the article.

References

[1] L. Voorwerk, M. Slagter, H.M. Horlings, K. Sikorska, K.K. van de Vijver, M. de Maaker, I. Nederlof, R.J.C. Kluin, S. Warren, S. Ong, T.G. Wiersma, N.S. Russell, F. Lalezari, P.C. Schouten, N.A.M. Bakker, S.L.C. Ketelaars, D. Peters, C.A.H. Lange, E. van Werkhoven, H. van Tinteren, I.A.M. Mandjes, I. Kemper, S. Onderwater, M. Chalabi, S. Wilgenhof, J. Haanen, R. Salgado, K.E. de Visser, G.S. Sonke, L.F. A. Wessels, S.C. Linn, T.N. Schumacher, C.U. Blank, M. Kok, Immune induction strategies in metastatic triple-negative breast cancer to enhance the sensitivity to PD-1 blockade: the TONIC trial, Nat Med 25 (6) (2019) 920–928.

[2] M. Yi, Y. Wu, M. Niu, S. Zhu, J. Zhang, Y. Yan, P. Zhou, Z. Dai, K. Wu, Anti-TGF-β/PD-L1 bispecific antibody promotes T cell infiltration and exhibits enhanced antitumor activity in triple-negative breast cancer, J Immunother Cancer 10 (12) (2022).

[3] S. Vranic, F.S. Cyprian, Z. Gatalica, J. Palazzo, PD-L1 status in breast cancer: current view and perspectives, Semin. Cancer Biol. 72 (2021) 146–154.

[4] F. Ye, S. Dewanjee, Y. Li, N.K. Jha, Z.S. Chen, A. Kumar, Vishakha, T. Behl, S. K. Jha, H. Tang, Advancements in clinical aspects of targeted therapy and immunotherapy in breast cancer, Mol. Cancer 22 (1) (2023) 105.

[5] D.S. Chen, I. Mellman, Elements of cancer immunity and the cancer-immune set point, Nature 541 (7637) (2017) 321–330.

[6] D. Hu, Z. Li, B. Zheng, X. Lin, Y. Pan, P. Gong, W. Zhuo, Y. Hu, C. Chen, L. Chen, J. Zhou, L. Wang, Cancer-associated fibroblasts in breast cancer: challenges and opportunities, Cancer Commun. 42 (5) (2022) 401–434.

[7] H. Wang, L. Wei, D. Mao, X. Che, X. Ye, Y. Liu, Y. Chen, Combination of oxymatrine (Om) and astragaloside IV (As) enhances the infiltration and function of TILs in triple-negative breast cancer (TNBC), Int. Immunopharmacol. 125 (Pt A) (2023) 111026.

[8] J. Guo, H. Zeng, X. Shi, T. Han, Y. Liu, Y. Liu, C. Liu, D. Qu, Y. Chen, A CFH peptide-decorated liposomal oxymatrine inactivates cancer-associated fibroblasts of hepatocellular carcinoma through epithelial-mesenchymal transition reversion, J Nanobiotechnology 20 (1) (2022) 114.

[9] X. Lan, J. Zhao, Y. Zhang, Y. Chen, Y. Liu, F. Xu, Oxymatrine exerts organ- and tissue-protective effects by regulating inflammation, oxidative stress, apoptosis, and fibrosis: from bench to bedside, Pharmacol. Res. 151 (2020) 104541.

[10] Y. Jin, Q. Yang, L. Liang, L. Ding, Y. Liang, D. Zhang, B. Wu, T. Yang, H. Liu, T. Huang, H. Shen, H. Tu, Y. Pan, Y. Wei, Y. Yang, F. Zhou, Compound kushen injection suppresses human acute myeloid leukaemia by regulating the Prdxs/ROS/Trx1 signalling pathway, J. Exp. Clin. Cancer Res. 37 (1) (2018) 277.

[11] W. Wang, R.L. You, W.J. Qin, L.N. Hai, M.J. Fang, G.H. Huang, R.X. Kang, M.H. Li, Y.F. Qiao, J.W. Li, A.P. Li, Anti-tumor activities of active ingredients in compound kushen injection, Acta Pharmacol. Sin. 36 (6) (2015) 676–679.

[12] H. Guo, Y. Liu, X. Li, H. Wang, D. Mao, L. Wei, X. Ye, D. Qu, J. Huo, Y. Chen, Magnetic metal-organic framework-based nanoplatform with platelet membrane coating as a synergistic programmed cell death protein 1 inhibitor against hepatocellular carcinoma, ACS Nano 17 (23) (2023) 23829–23849.

[13] B. Li, Y. Hu, T. Wu, Y. Feng, C. Jiang, H. Du, S. Lu, Apigenin-oxymatrine binary co-amorphous mixture: enhanced solubility, bioavailability, and anti-inflammatory effect, Food Chem. 373 (Pt B) (2022) 131485.

[14] J. Peng, Q. Wang, M. Guo, C. Liu, X. Chen, L. Tao, K. Zhang, X. Shen, Development of inhalable chitosan-coated oxymatrine liposomes to alleviate RSV-infected mice, Int. J. Mol. Sci. 23 (24) (2022).

[15] A. Sheik, K. Kim, G.L. Varaprasad, H. Lee, S. Kim, E. Kim, J.Y. Shin, S.Y. Oh, Y. S. Huh, The anti-cancerous activity of adaptogenic herb Astragalus membranaceus, Phytomedicine 91 (2021) 153698.

[16] Z. Gu, C.G. Da Silva, Y. Hao, T. Schomann, M.G.M. Camps, K. van der Maaden, Q. Liu, F. Ossendorp, L.J. Cruz, Effective combination of liposome-targeted chemotherapy and PD-L1 blockade of murine colon cancer, J Control Release 353 (2023) 490–506.

[17] F. Xu, M. Li, Z. Que, M. Su, W. Yao, Y. Zhang, B. Luo, Y. Li, Z. Zhang, J. Tian, Combined chemo-immuno-photothermal therapy based on ursolic acid/astragaloside IV-loaded hyaluronic acid-modified polydopamine nanomedicine inhibiting the growth and metastasis of non-small cell lung cancer, J. Mater. Chem. B 11 (15) (2023) 3453–3472.

[18] Y. Xi, W. Wang, L. Ma, N. Xu, C. Shi, G. Xu, H. He, W. Pan, Alendronate modified mPEG-PLGA nano-micelle drug delivery system loaded with astragaloside has anti-osteoporotic effect in rats, Drug Deliv. 29 (1) (2022) 2386–2402.

[19] Q. Tang, W. Zhang, C. Zhang, Y. Guan, J. Ding, C. Yuan, C. Tan, X. Gao, S. Tan, Oxymatrine loaded nitric oxide-releasing liposomes for the treatment of ulcerative colitis, Int J Pharm 586 (2020) 119617.

[20] Y. Li, T. Ji, M. Torre, R. Shao, Y. Zheng, D. Wang, X. Li, A. Liu, W. Zhang, X. Deng, R. Yan, D.S. Kohane, Aromatized liposomes for sustained drug delivery, Nat. Commun. 14 (1) (2023) 6659.

[21] C.W.t. Shields, L.L. Wang, M.A. Evans, S. Mitragotri, Materials for immunotherapy, Adv Mater 32 (13) (2020) e1901633.

[22] M. Liu, S. Jin, H. Yan, S. Du, Effect of oxymatrine HSPC liposomes on improving bioavailability, liver target distribution and hepatoprotective activity of oxymatrine, Eur J Pharm Sci 104 (2017) 212–220.

[23] Y.C. Kuo, I.Y. Chen, R. Rajesh, Astragaloside IV- and nesfatin-1-encapsulated phosphatidylserine liposomes conjugated with wheat germ agglutinin and leptin to activate anti-apoptotic pathway and block phosphorylated tau protein expression for Parkinson's disease treatment, Mater Sci Eng C Mater Biol Appl 129 (2021) 112361.

[24] Y. Zhang, C. Sun, C. Wang, K.E. Jankovic, Y. Dong, Lipids and lipid derivatives for RNA delivery, Chem Rev 121 (20) (2021) 12181–12277.

[25] M.D. Fulton, W. Najahi-Missaoui, Liposomes in cancer therapy: how did we start and where are we now, Int. J. Mol. Sci. 24 (7) (2023).

[26] A.A. Gabizon, R.T.M. de Rosales, N.M. La-Beck, Translational considerations in nanomedicine: the oncology perspective, Adv. Drug Deliv. Rev. 158 (2020) 140–157.

[27] R. Al-Kassas, M. Bansal, J. Shaw, Nanosizing techniques for improving bioavailability of drugs, J Control Release 260 (2017) 202–212.

[28] S.H. El Moukhtari, E. Garbayo, A. Amundarain, S. Pascual-Gil, A. Carrasco-León, F. Prosper, X. Agirre, M.J. Blanco-Prieto, Lipid nanoparticles for siRNA delivery in cancer treatment, J Control Release 361 (2023) 130–146.

[29] A.H. Colby, R. Liu, R.P. Doyle, A. Merting, H. Zhang, N. Savage, N.Q. Chu, B. A. Hollister, W. McCulloch, J.E. Burdette, C.J. Pearce, K. Liu, N.H. Oberlies, Y. L. Colson, M.W. Grinstaff, Pilot-scale production of expansile nanoparticles: practical methods for clinical scale-up, J Control Release 337 (2021) 144–154.

[30] Y. Wang, Y. Zheng, L. Zhang, Q. Wang, D. Zhang, Stability of nanosuspensions in drug delivery, J Control Release 172 (3) (2013) 1126–1141.

[31] L. Liu, W. Wang, W. Hong, Y. Jin, L. Wang, S. Liu, A. Wang, X. Liu, Photothermal 2D nanosheets combined with astragaloside IV for antibacterial properties and promoting angiogenesis to treat infected wounds, Front. Bioeng. Biotechnol. 9 (2021) 826011.

[32] S. Shah, V. Dhawan, R. Holm, M.S. Nagarsenker, Y. Perrie, Liposomes: advancements and innovation in the manufacturing process, Adv. Drug Deliv. Rev. 154–155 (2020) 102–122.

[33] K. Eyer, F. Paech, F. Schuler, P. Kuhn, R. Kissner, S. Belli, P.S. Dittrich, S.D. Krämer, A liposomal fluorescence assay to study permeation kinetics of drug-like weak bases across the lipid bilayer, J Control Release 173 (2014) 102–109.

[34] H. Wang, Y. Ding, W. Zhang, K. Wei, Y. Pei, C. Zou, C. Zhang, J. Ding, H. Fang, S. Tan, Oxymatrine liposomes for intervertebral disc treatment: formulation, in vitro and vivo assessments, Drug Des Devel Ther 14 (2020) 921–931.

[35] K. Jebastin, D. Narayanasamy, Rationale utilization of phospholipid excipients: a distinctive tool for progressing state of the art in research of emerging drug carriers, J. Liposome Res. 33 (1) (2023 Mar) 1–33.

[36] C.C.L. Cheung, W.T. Al-Jamal, Sterically stabilized liposomes production using staggered herringbone micromixer: effect of lipid composition and PEG-lipid content, Int J Pharm 566 (2019) 687–696.

[37] N. Filipczak, J. Pan, S.S.K. Yalamarty, V.P. Torchilin, Recent advancements in liposome technology, Adv. Drug Deliv. Rev. 156 (2020) 4–22.

[38] H. Zhang, J. Yang, R. Sun, S. Han, Z. Yang, L. Teng, Microfluidics for nano-drug delivery systems: from fundamentals to industrialization, Acta Pharm. Sin. B 13 (8) (2023) 3277–3299.

[39] (CDER), U. S. D. O. H. a. H. S. F. a. D. A. C. F. D. E. a. R., Lipsomes Drug Products Chemistry,manufacturing,and Controls; Human Pharmacokinetics and Bioavailability; and Labeling Documentation, 2018.

[40] V.G.S. Sainaga Jyothi, R. Bulusu, B. Venkata Krishna Rao, M. Pranothi, S. Banda, P. Kumar Bolla, N. Kommineni, Stability characterization for pharmaceutical liposome product development with focus on regulatory considerations: an update, Int J Pharm 624 (2022 Aug 25) 122022.

[41] G. Yang, Y. Liu, C.X. Zhao, Quantitative comparison of different fluorescent dye-loaded nanoparticles, Colloids Surf. B Biointerfaces 206 (2021) 111923.

[42] C. Åberg, Kinetics of nanoparticle uptake into and distribution in human cells, Nanoscale Adv. 3 (8) (2021) 2196–2212.

[43] Y. Zhu, X. Zhu, C. Tang, X. Guan, W. Zhang, Progress and challenges of immunotherapy in triple-negative breast cancer, Biochim. Biophys. Acta Rev. Canc 1876 (2) (2021) 188593.

[44] Y. Wang, C. Wang, J. Qiu, X. Qu, J. Peng, C. Lu, M. Zhang, M. Zhang, X. Qi, G. Li, K. Hua, Targeting CD96 overcomes PD-1 blockade resistance by enhancing CD8+ TIL function in cervical cancer, J Immunother Cancer 10 (3) (2022).

[45] Y. Wu, Z. Yi, J. Li, Y. Wei, R. Feng, J. Liu, J. Huang, Y. Chen, X. Wang, J. Sun, X. Yin, Y. Li, J. Wan, L. Zhang, J. Huang, H. Du, X. Wang, Q. Li, G. Ren, H. Li, FGFR blockade boosts T cell infiltration into triple-negative breast cancer by regulating cancer-associated fibroblasts, Theranostics 12 (10) (2022) 4564–4580.

[46] R.I.K. Geltink, R.L. Kyle, E.L. Pearce, Unraveling the complex interplay between T cell metabolism and function, Annu. Rev. Immunol. 36 (2018 Apr 26) 461–488.

[47] S.A. Vardhana, M.A. Hwee, M. Berisa, D.K. Wells, K.E. Yost, B. King, M. Smith, P. S. Herrera, H.Y. Chang, A.T. Satpathy, M.R.M. van den Brink, J.R. Cross, C. B. Thompson, Impaired mitochondrial oxidative phosphorylation limits the self-renewal of T cells exposed to persistent antigen, Nat. Immunol. 21 (9) (2020 Sep) 1022–1033.

[48] A. Śledzińska, M. Vila de Mucha, K. Bergerhoff, A. Hotblack, D.F. Demane, E. Ghorani, A.U. Akarca, M.A.V. Marzolini, I. Solomon, F.A. Vargas, M. Pule, M. Ono, B. Seddon, G. Kassiotis, C.E. Ariyan, T. Korn, T. Marafioti, G.M. Lord, H. Stauss, R.G. Jenner, K.S. Peggs, S.A. Quezada, Regulatory T cells restrain interleukin-2- and blimp-1-dependent acquisition of cytotoxic function by CD4 T cells, Immunity 52 (1) (2020 Jan 14) 151–166.e6.

[49] L. Jenkins, U. Jungwirth, A. Avgustinova, M. Iravani, A. Mills, S. Haider, J. Harper, C.M. Isacke, Cancer-associated fibroblasts suppress CD8+ T-cell infiltration and confer resistance to immune-checkpoint blockade, Cancer Res. 82 (16) (2022) 2904–2917.

[50] Y.R. Yu, H. Imrichova, H. Wang, T. Chao, Z. Xiao, M. Gao, M. Rincon-Restrepo, F. Franco, R. Genolet, W.C. Cheng, C. Jandus, G. Coukos, Y.F. Jiang, J.W. Locasale, A. Zippelius, P.S. Liu, L. Tang, C. Bock, N. Vannini, P.C. Ho, Disturbed

mitochondrial dynamics in CD8(+) TILs reinforce T cell exhaustion, Nat. Immunol. 21 (12) (2020) 1540–1551.

[51] J.F. Yang, X. Xing, L. Luo, X.W. Zhou, J.X. Feng, K.B. Huang, H. Liu, S. Jin, Y. N. Liu, S.H. Zhang, Y.H. Pan, B. Yu, J.Y. Yang, Y.L. Cao, Y. Cao, C.Y. Yang, Y. Wang, Y. Zhang, J. Li, X. Xia, T. Kang, R.H. Xu, P. Lan, J.H. Luo, H. Han, F. Bai, S. Gao, Mitochondria-ER contact mediated by MFN2-SERCA2 interaction supports CD8(+) T cell metabolic fitness and function in tumors, Sci Immunol 8 (87) (2023) eabq2424.

[52] P. Wong, J.A. Foltz, L. Chang, C.C. Neal, T. Yao, C.C. Cubitt, J. Tran, S. Kersting-Schadek, S. Palakurty, N. Jaeger, D.A. Russler-Germain, N.D. Marin, M. Gang, J. A. Wagner, A.Y. Zhou, M.T. Jacobs, M. Foster, T. Schappe, L. Marsala, E. McClain, P. Pence, M. Becker-Hapak, B. Fisk, A.A. Petti, O.L. Griffith, M. Griffith, M. M. Berrien-Elliott, T.A. Fehniger, T-BET and EOMES sustain mature human NK cell identity and antitumor function, J. Clin. Investig. 133 (13) (2023).

[53] A.M. Intlekofer, N. Takemoto, E.J. Wherry, S.A. Longworth, J.T. Northrup, V. R. Palanivel, A.C. Mullen, C.R. Gasink, S.M. Kaech, J.D. Miller, L. Gapin, K. Ryan, A.P. Russ, T. Lindsten, J.S. Orange, A.W. Goldrath, R. Ahmed, S.L. Reiner, Effector and memory CD8+ T cell fate coupled by T-bet and eomesodermin, Nat. Immunol. 6 (12) (2005) 1236–1244.

[54] R. Yang, F. Mele, L. Worley, D. Langlais, J. Rosain, I. Benhsaien, H. Elarabi, C. A. Croft, J.M. Doisne, P. Zhang, M. Weisshaar, D. Jarrossay, D. Latorre, Y. Shen, J. Han, M. Ogishi, C. Gruber, J. Markle, F. Al Ali, M. Rahman, T. Khan, Y. Seeleuthner, G. Kerner, L.T. Husquin, J.L. Maclsaac, M. Jeljeli, A. Errami, F. Ailal, M.S. Kobor, C. Oleaga-Quintas, M. Roynard, M. Bourgey, J. El Baghdadi, S. Boisson-Dupuis, A. Puel, F. Batteux, F. Rozenberg, N. Marr, Q. Pan-Hammarström, D. Bogunovic, L. Quintana-Murci, T. Carroll, C.S. Ma, L. Abel, A. Bousfiha, J.P. Di Santo, L.H. Glimcher, P. Gros, S.G. Tangye, F. Sallusto, J. Bustamante, J.L. Casanova, Human T-bet governs innate and innate-like adaptive IFN-γ immunity against mycobacteria, Cell 183 (7) (2020) 1826–1847. e31.

[55] V. Lazarevic, L.H. Glimcher, T-bet in disease, Nat. Immunol. 12 (7) (2011) 597–606.

[56] T. Kanazawa, W. Sato, B.J.E. Raveney, D. Takewaki, A. Kimura, H. Yamaguchi, Y. Yokoi, R. Saika, Y. Takahashi, T. Fujita, S. Saiki, A. Tamaoka, S. Oki, T. Yamamura, Pathogenic potential of eomesodermin-expressing T-helper cells in neurodegenerative diseases, Ann. Neurol. 95 (6) (2024) 1093–1098.

[57] X.Q. Wang, E. Danenberg, C.S. Huang, D. Egle, M. Callari, B. Bermejo, M. Dugo, C. Zamagni, M. Thill, A. Anton, S. Zambelli, S. Russo, E.M. Ciruelos, R. Greil, B. Győrffy, V. Semiglazov, M. Colleoni, C.M. Kelly, G. Mariani, L. Del Mastro, O. Biasi, R.S. Seitz, P. Valagussa, G. Viale, L. Gianni, G. Bianchini, H.R. Ali, Spatial predictors of immunotherapy response in triple-negative breast cancer, Nature 621 (7980) (2023) 868–876.